Chemical evolution of atmospheric organic carbon over multiple generations of oxidation

Citation: Isaacman-VanWertz et al. "Chemical Evolution of Atmospheric Organic Carbon over Multiple Generations of Oxidation." Nature Chemistry 10, no. 4 (February 26, 2018): 462–468.

As Published: http://dx.doi.org/10.1038/s41557-018-0002-2

Publisher: Nature Publishing Group

Persistent URL: http://hdl.handle.net/1721.1/119485

Version: Final published version: final published article, as it appeared in a journal, conference proceedings, or other formally published context

Chemical evolution of atmospheric organic carbon over multiple generations of oxidation

Gabriel Isaacman-VanWertz[1,2]*, Paola Massoli[3], Rachel O'Brien[1], Christopher Lim[1], Jonathan P. Franklin[1], Joshua A. Moss[1], James F. Hunter[1], John B. Nowak[3,#], Manjula R. Canagaratna[3], Pawel K. Misztal[4], Caleb Arata[4], Joseph R. Roscioli[3], Scott T. Herndon[3], Timothy B. Onasch[3], Andrew T. Lambe[3], John T. Jayne[3], Luping Su[5], Daniel A. Knopf[5], Allen H. Goldstein[4], Douglas R. Worsnop[3], Jesse H. Kroll[1]*

[1]Department of Civil and Environmental Engineering, Massachusetts Institute of Technology, Cambridge, Massachusetts 02139, USA

[2]Department of Civil and Environmental Engineering, Virginia Tech, Blacksburg, Virginia 24061, USA

[3]Aerodyne Research Inc., Billerica, Massachusetts 01821, USA

[4]Department of Environmental Science, Policy, and Management, University of California, Berkeley, California 94720, USA

[5]School of Marine and Atmospheric Sciences, Stony Brook University, Stony Brook, New York 11794, USA

[#]Now at NASA Langley Research Center, Hampton, VA 23681, USA

Table of Contents Summary: We quantify and characterize nearly all organic carbon in a highly complex evolving atmospheric system: the multi-generational oxidation of a-pinene. We observe that initial addition of functional groups quickly gives way to fragmentation reactions, with organic carbon ultimately becoming sequestered in chemically-resistant reservoirs: organic aerosol and long-lived gas-phase species.

Abstract

The evolution of atmospheric organic carbon (OC) as it undergoes oxidation has a controlling influence on concentrations of key atmospheric species, including particulate matter, ozone, and oxidants. However, full characterization of OC over hours to days of atmospheric processing has been stymied by its extreme chemical complexity. Here we study the multigenerational oxidation of α-pinene in the laboratory, characterizing products with several state-of-the-art analytical techniques. While quantification of some early-generation products remains elusive, full carbon closure is achieved (within measurement uncertainty) by the end of the experiments. These results provide new insights into the effects of oxidation on OC properties (volatility, oxidation state, and reactivity) and the atmospheric lifecycle of OC. Following an initial period characterized by functionalization reactions and particle growth, fragmentation reactions dominate, forming smaller species. After approximately one day of atmospheric aging, most carbon is sequestered in two long-lived reservoirs, volatile oxidized gases and low-volatility particulate matter.

Organic compounds play a central role in the chemistry of the atmosphere, by contributing to ozone formation,[1,2] serving as the primary sink for oxidants in the atmosphere,[3,4] and constituting a substantial fraction of global submicron particulate matter.[5,6] Organic carbon (OC) enters the atmosphere primarily as high-volatility gases. Oxidation of these compounds yields a large number of products, including organic species in the gas phase (gas-phase OC, gOC), organic species in the condensed phase (particle-phase OC, pOC), and inorganic carbon-containing species (CO and CO_2). All of these products (other than CO_2) may themselves undergo further oxidation, continuing this process over multiple generations to produce a highly complex, chemically dynamic mixture of compounds that spans a wide range in chemical composition and properties (e.g., volatility).[7–11] Oxidation continues until OC is either converted to CO_2, or removed from the atmosphere through deposition to the Earth's surface, thereby transporting a wide range of organic compounds into other components of the Earth system. Our ability to track the oxidative evolution of OC over its entire atmospheric lifetime therefore controls not only our ability to understand critical issues in air quality and atmospheric chemistry, but ultimately to understand the impacts of organic emissions on human health, ecosystems, and Earth's climate.

The comprehensive measurement of all oxidation products from a given chemical system has been elusive due to the analytical challenges associated with detecting, characterizing, and quantifying compounds within complex organic mixtures. Only studies of the simplest organic compounds have achieved "carbon closure," fully characterizing the product mixture throughout oxidation.[12] For larger species, a large fraction of the products has remained unmeasured and/or uncharacterized, even in the early stages of reaction (first 1-2 generations of oxidation).[13,14] As a result, there is substantial uncertainty as to the fate and impact of OC over timescales longer than several hours after emission. For example, the possibility of substantial unmeasured "pools" of OC has major implications for the formation of particle-phase mass through the gas-to-particle partitioning of condensable gases. It has traditionally been assumed that such unmeasured carbon will not condense to contribute to particle-phase mass. However, if instead unmeasured carbon in laboratory experiments is irreversibly lost to chamber walls via vapor deposition[15] or reacts over multiple generations to form lower-volatility gases,[9,16] then formation of pOC from many precursors may be substantially higher than currently estimated. The properties and reactivity of organic oxidation products formed over multiple generations will also impact ozone production, removal pathways (e.g. wet and dry deposition) of pollutants, and reactivity and cycling of oxidants. A quantitative, predictive description of these processes across spatial scales therefore relies critically on the measurement of the chemistry of such species, and more generally on our ability to measure and track all OC in a reactive system.

Here, we apply recent advances in analytical instrumentation to characterize the full mixture of products formed in hydrocarbon oxidation with the goal of achieving carbon closure, enabling a more complete understanding of the chemical properties and transformation processes of atmospheric OC. We access the entire range of expected chemical properties of suspended products[17] with an array of state-of-the-art analytical instruments: an aerosol mass spectrometer[18] (TD-AMS) and scanning mobility particle sizer (SMPS) to measure pOC with volatility resolution, a proton transfer reaction mass spectrometer[19,20] (PTR-MS) and two chemical ionization mass spectrometers[21] (I^- CIMS and NO_3^- CIMS[22–25]) to measure gOC, and two tunable infrared laser differential absorption spectrometers (TILDAS) to measure C_1 compounds (CO, formaldehyde, and formic acid). We combine the data from these instruments to present a unified, time-resolved description of the chemical composition of two oxidation systems: initial oxidation of α-pinene (a monoterpene) through photooxidation by hydroxyl radicals (OH) in the

presence of NO, and ozonolysis in the absence of NO, followed in both cases by continued high-NO OH oxidation. All experiments were performed at 20 °C and low relative humidity (<5%); see Methods and Supplementary Sect. 1 for details on reaction conditions and instrument operation, calibration, and uncertainty. These systems were chosen because their initial chemistry has been subject to extensive theoretical and experimental characterization,[26–28] but the subsequent multi-generational oxidation ("aging") of the reaction mixture (particularly gOC) has received substantially less study.[29] By the end of the experiments, all carbon is measured to within experimental uncertainties, enabling a coherent and detailed picture of the chemical evolution of the product mixture, and providing new insights into the lifecycle and fate of atmospheric OC.

Results

Carbon closure

All products measured in the OH-initiated oxidation of α-pinene are shown in Fig. 1. Results are qualitatively similar to those in the ozonolysis experiment, so ozonolysis results are given in Supplementary Sect. 5. Initial reaction of α-pinene is immediately accompanied by a concomitant rise in in both gOC and pOC oxidation products. Particle-phase OC is formed in the first generations of oxidation, with only minor additional formation after the α-pinene is fully consumed, and accounts for 14±3% of the total carbon by the end of the experiment (~24 hours of equivalent daytime atmospheric oxidation). We focus our characterization of pOC on average chemical properties and volatility distributions, providing an ensemble description of the aerosol, while composition of gOC is characterized by individual species. Identified gas-phase products are CO, formaldehyde, formic acid, acetic acid, acetone, and pinonaldehyde. Concentrations of each identified product vary over the course of the experiment, but in total account for 41±5% of the carbon by the end. CO_2 is not measured here but is expected to be similar in concentration to CO (~4%).[30]

In addition to known compounds, chemical species measured include a large number of "unidentified" gas-phase reaction products, detected by the gas-phase mass spectrometers as 310 ions. Structures for these ions cannot be unambiguously assigned, but molecular formulas are known, from which chemical properties (e.g. volatility) can be estimated using group contribution methods.[31] These unidentified species comprise 46±17% of the carbon at the end of the experiment, most of which is measured by PTR-MS and I^- CIMS. Species measured by the NO_3^- CIMS (extremely low volatility, highly oxidized gases)[32] account for <0.5% of the total carbon, and so are not included in Fig. 1. The overlap between carbon measured by each instrument is minor, with ions of the same formulas measured by different instruments accounting for less than 20 ppbC (4% of carbon, see Methods). The dominant single contributor to unidentified carbon is $C_3H_4O_4$ (yield of ~5%, measured by I^- CIMS), which has previously been observed in the atmosphere and identified as malonic acid;[33] however, its ion cluster strength (Supplementary Fig. 1) indicates that it is not malonic acid but rather some isomer (or combination of isomers) thereof (e.g., the modeled pinene oxidation product 3-oxo-peroxypropanoic acid[34]). This highlights the need for new measurements that provide information on molecular structure and improved characterization of these unidentified species.[35] Off-line techniques that would provide this information (e.g. tandem mass spectrometry) tend not to be adapted for the direct analysis of these gas-phase compounds, which may undergo chemical transformations upon collection or extraction.

The total measured carbon yield is 102±20% (1σ) by the end of the experiment. Calibrations of individual ions are relatively uncertain (e.g., a factor of 2.5 per ion in the I^- CIMS) because authentic standards are

not available for most species. However, uncertainties in each ion are primarily due to random deviations from average calibration relationships rather than systematic bias; relative uncertainty for total measured carbon is therefore lower than that for any given ion and is calculated by the quadrature addition of individual absolute uncertainties. The contributions of each instrument to total uncertainty is provided in the Methods, and given in detail in Supplementary Table 1. "Carbon closure" is achieved in this experiment within measurement uncertainties, allowing for a more comprehensive characterization of the evolving carbon distribution over these timescales than previously possible. This also indicates that the loss of condensable carbon to chamber walls or other surfaces is not a major sink for reaction products in this experiment, as expected given the fast rate of oxidation and the use of seed particles as a condensation sink,[36–38] and supported by modeled gas-particle-wall partitioning (Supplementary Sect. 4).

Not all carbon is measured throughout the entire experiment; some "missing" carbon (up to ~40%) is unmeasured early in the experiment. The time dependence of this unmeasured carbon suggests it is made up of early-generation products that quickly react away (with a ~4h timescale) to yield measured products, leading to the observed carbon closure by the end of the experiment. These unmeasured species may be compounds that are not readily detected by the instrument suite. For example, the one peak in the I^- CIMS mass spectrum that is above the detection limit but substantially below the threshold for reliable instrument calibration (and hence not included in Fig. 1) is $C_{10}H_{17}NO_4$ (Supplementary Fig. 2). This likely corresponds to α-pinene hydroxynitrate, a first-generation oxidation product known to be formed in high yields (~15%), but that is not sensitively measured by any of the present instruments.[27,39] Importantly, the temporal behavior and ion intensity of this species (after applying an approximate calibration factor[40]) matches the unmeasured carbon well (Supplementary Sect. 4). "Missing" carbon is also observed in the ozonolysis experiment (Supplementary Sect. 5), for which no nitrate formation is expected, so it appears that this instrument suite is not generally sensitive to lightly-oxidized, lower-volatility gases, leading to poor carbon closure in the early generations of oxidation. In addition to undetected or poorly-detected ions, unmeasured carbon may include underestimation of low-sensitivity isomers of detected ions, which is particularly likely for isomers of lightly functionalized ions (Supplementary Sect. 2). Early-generation compounds, comprising gases of relatively low volatility, may also reversibly partition to reactor or inlet walls[41] and re-volatilize upon reaction of their gas-phase component with OH, which could also contribute to unmeasured carbon early in the experiment. Thus, despite uncertainties related to its molecular identity, the unmeasured carbon is likely comprised of lightly oxidized, relatively low volatility gas-phase products. Indeed, this unmeasured carbon correlates well with the least-oxygenated measured ions (Supplementary Fig. 4). Moreover, the majority of the OC (and all of it by the end of the experiment) is quantified and characterized by chemical properties and formulas, providing a unique opportunity to examine the evolution of the composition and chemistry of OC over multiple generations of oxidation.

Evolving properties of the carbon

The changing composition of this complex mixture with oxidation is shown in Fig. 2, as three "snapshots" of the product distribution in terms of carbon oxidation state ($\overline{OS_C}$), vs. volatility (expressed as saturation concentration, c^*), often referred to as the "two-dimensional volatility basis set".[10,42] Carbon in the first hour of the experiment (Fig. 2a) is dominated by the precursor, α-pinene, and the formation of products with intermediate volatility ($c^* = 10^3$-10^6 μg m^{-3}), as well as some higher-volatility gases (e.g., acetone, acetic acid), and particle-phase mass. By the end of the initial oxidation, after

nearly all α-pinene has reacted (Fig. 2b), the product mixture spans a wide range of volatilities and oxidation states. Upon further oxidation (Fig. 2c), the distribution of products changes further, indicating the importance of continuing oxidation chemistry beyond the initial α-pinene oxidation.

In this chemically dynamic system, the behavior of different products is determined by both their formation pathways and their lifetime versus further oxidation by OH. Some early-generation products, including most intermediate-volatility organic compounds (IVOCs; e.g., pinonaldehyde and multi-functional nitrates), exhibit rapid decreases in concentration after formation, consistent with their high reactivity.[43,44] By contrast, concentrations of some of the volatile compounds (e.g., CO and acetone) consistently increase throughout the experiment. These are formed both from the initial oxidation of α-pinene as well as from the multigenerational oxidation of reaction products, and their slow reaction rates with OH preclude any significant decay over the timescales of the experiment. This category of less-reactive products also includes pOC, which increases throughout the experiment with only relatively minor changes in average properties, consistent with the long lifetime of particulate carbon against heterogeneous oxidation by gas-phase oxidants.[45,46]

The evolution of the organic mixture as a whole can be described in terms of changes to key chemical properties of the measured products. Figure 3 shows the evolving distributions of three such properties: carbon number (n_C), $\overline{\mathrm{OS_C}}$, and c^*. The n_C of observed products (Fig. 3a) exhibits a clear and dramatic change with oxidation: C_{10} species make up a large fraction (~50%, likely an underestimate since the early-generation unmeasured species are expected to be C_{10}), indicating the importance of functionalization reactions (addition of oxygen-containing groups) early in the reaction. These reactions contribute to the early formation of pOC via gas-to-particle conversion and in-particle accretion reactions that yield low volatility products. However, trends in chemical properties are dominated by gOC, which is the majority fraction of carbon. (The individual trends for pOC and gOC are shown in Supplementary Fig. 6). Further oxidation depletes gas-phase C_{10} compounds, which account for only 12% of the carbon by the end of the experiment. Their oxidation produces species with smaller carbon numbers (in particular $C_{1\text{-}3}$), suggesting that later-generation oxidation is dominated by fragmentation reactions. The $\overline{\mathrm{OS_C}}$ distribution of the product mixture (Fig. 3b) is initially dominated by species with low (<-0.5) oxidation states, but further oxidation leads to the formation of higher oxidation state products, including very oxidized products with oxidation state > +1 (e.g. formic acid and CO) and a few less-oxidized species (mostly acetone).

The volatility distribution (Fig. 3c) also undergoes major changes. Initial product carbon is dominated by gas-phase IVOCs, C_{10} products formed by the addition of 1-3 functional groups to the carbon skeleton of the precursor. An early drop in volatility is observed because initially formed products include low-volatility pOC, which is measured, and intermediate-volatility gOC, which is partly unmeasured. As gas-phase species oxidize, the distribution of volatilities shifts away from IVOCs, toward both higher- and lower-volatility products. By the end of the experiment, IVOCs represent a small fraction of the total carbon, which is instead dominated by high-volatility gases (formed from fragmentation reactions) or pOC (formed mostly from functionalization reactions). The trends observed in Fig. 3 are further enhanced by including α-pinene (Supplementary Fig. 6) or unmeasured species, as those have chemical properties similar to early-generation products (large, moderately volatile, and lightly oxidized). Ozonolysis experiment exhibits the same trends as the photooxidation, but with fewer changes during the initial oxidation, since the initial reaction ceases after the oxidation of the double bonds.

The evolution of the organic mixture, in which the early-generation species (mostly large, lightly-oxidized, intermediate-volatility species) react to form small, volatile species in the gas phase and low-volatility species in the particle phase, has important implications for the evolving reactivity and lifetime of atmospheric OC. Figure 4a shows the changes to the distribution of the atmospheric lifetime against reaction with OH (τ_{ox}) of the product mixture. Functionalized IVOCs generally have lifetimes of only 3-9 hours, so the lifetimes of initial products are generally short.[45] Unmeasured carbon, representing one or a distribution of several such compounds, is included in Fig. 4 with a lifetime of the observed decay timescale (~4 hours, time-dependence of unmeasured mass shown in Supplementary Fig. 9).

While the initial IVOC products are short lived with respect to oxidation, other products are extremely long-lived, such as CO (τ_{ox} = 39 days[47]), acetone (τ_{ox} = 34 days[48]), and pOC (τ_{ox} = 69 days[46]). Over the course of the experiment, the IVOCs react away and these longer-lived species continue to grow in, increasing the average lifetime of products in the mixture from 5 hours to 2 days. By the end of the experiment, more than half of the carbon is in species that are sufficiently long-lived (τ_{ox} > 20 hrs) to be unreactive on the timescale of the experiment. This tendency toward long-lived species is a natural consequence of any multigenerational reaction system, since less-reactive products represent "kinetic bottlenecks" and hence will necessarily accumulate. Reversible deposition to walls may impact the timescale of the reaction in this work by temporarily sequestering some reactive carbon from oxidation by OH, but these processes will not substantially diminish the kinetic tendency toward less-reactive products. In the present system, this tendency is closely correlated with the evolving volatility distributions, since long-lived species tend either to be small gas-phase oxygenates (e.g., CO, acetone), or present in the condensed phase (as pOC). Thus, within approximately a day of atmospheric aging of this system, the volatility distribution of the product mixture becomes bimodal, dominated by particles and long-lived high-volatility gases (Fig. 4b). This decrease in reactivity through sequestration of carbon in "low-reactivity pools" occurs roughly exponentially, with a characteristic time of ~3 hours (Fig. 4c); this timescale matches the approximate lifetime of the first-generation products that drive the initial reactivity of the product mixture. Chemical systems are expected to vary in their timescales and composition depending on reaction rates of reactants and products, and the impacts of other chemical processes (e.g. aqueous and multi-phase reactions), but the tendency toward long-lived products is expected for most atmospheric systems.

Discussion

By characterizing nearly all the products formed in a complex chemical system in terms of their molecular formulas and physicochemical properties, we have been able to examine the products and evolution of atmospheric OC through multi-generational oxidation. Initial oxidation occurs through the addition of functional groups to form pOC mass and large, intermediate-volatility gases, but upon further oxidation gas-phase products quickly fragment into high-volatility compounds. Particulate carbon and some oxidized volatile gases are resistant to further oxidation by OH, so carbon effectively becomes sequestered in these two pools. The present results are limited to the oxidation of a single precursor hydrocarbon, under a limited set of reaction conditions, and other chemical systems may exhibit somewhat different behavior. However, known long-lived products (e.g., pOC, formic acid, CO, etc.) are formed by a wide range of oxidation systems, and longer-lived species will necessarily accumulate over the course of multiple generations of oxidation. Thus the general trends shown in Fig. 4

– the eventual decrease in reactivity and the bifurcation in volatility – are likely to be common features of the oxidation of most atmospheric organic species. Ambient processes that are not captured by these experiments (e.g. aqueous-phase reactions, in-particle secondary chemistry,[49] reactive uptake of soluble gases such as those formed from isoprene oxidation[50,51]) may increase the oxidation or fragmentation of pOC or alter chemical pathways. This would shift the relative balance between condensed-phase and high-volatility long-lived reservoirs, but is unlikely to substantially increase or change the trend in the overall reactivity of OC.

The observed timescale for oxidative removal of reactive gases and formation of long-lived species has broad implications for understanding the fate of atmospheric OC on global and regional scales. Near emission sources, the diverse and complex mixture of functionalized gases formed from emissions are likely to comprise a significant fraction of suspended carbon, playing a critical role in particle growth, OH reactivity, and depositional loss.[11,16,52–56] However, farther from emissions, IVOCs will be substantially depleted and most mass will be comprised of relatively few long-lived constituents, so composition and removal of OC in remote regions will be dominated by particles and C_{1-3} gases. Where an airmass is on the continuum between near- and far-field is a function of both the inherent timescales for oxidation of a given chemical system and the "average age" of the OC. Some approaches to quantify the average age of an airmass have been developed, but are generally limited to anthropogenically-influenced chemistries.[57,58] The fate of atmospheric OC is determined by the competition between the oxidation reactions studied, other chemical processes (e.g. aqueous-phase reactions) that may modify the oxidation pathways, and deposition. The relative timescales of each govern the extent to which emitted carbon is deposited as lightly-functionalized species before being sequestered by oxidation. The timescales of oxidation measured in this work therefore need to be complemented by better observational constraints on average age of OC and timescales of removal in order to improve understanding of the lifecycle and fate of OC under a range of atmospheric conditions.

Methods

Reaction conditions

Studies were carried out using a fixed-volume temperature-controlled 7.5 m^3 Teflon environmental chamber in which was mixed α-pinene (60 ppb), ammonium sulfate aerosol (~70 μg m^{-3}), and a non-reactive tracer used to measure dilution rate (hexafluorobenzene). Oxidant was introduced as ozone (~350 ppb), or HONO (50 ppb) in the presence of ultraviolet light (300-400 nm) to produce OH radicals. Multi-generational oxidation was initiated 4.5 hours after initial oxidation, through the introduction of ~2 ppb/min HONO in the presence of ultraviolet light. Reactions were carried out at 20 °C and low relative humidity (<5%). All data are corrected for dilution due to instrument sampling. Reported particle mass concentrations are corrected for loss to the walls using a rate calculated from the loss rate of seed particles prior to reaction. Additional details are provided in Supplementary Sect. 1.

Measurements

Detailed operation conditions and calibration methods are provided for all instruments in Supplementary Sect. 1. Four high-resolution ($m/\Delta m \approx 4000$) time-of-flight mass spectrometers (HTOF; Tofwerk AG) were used in this work: gas-phase composition was measured by PTR-MS[19,20] (Ionikon

Analytik) and two CIMS[21] (Aerodyne Research Inc.) using I^- and NO_3^- as reagent ions,[22–25] and particle-phase composition was measured by an AMS[18] (Aerodyne Research Inc.). The latter sampled downstream of a Thermal Denuder[59] to measure volatility distribution of particles. Two TILDAS[60] (Aerodyne Research Inc.) instruments measured C_1 compounds. Particle size distributions measured by Scanning Mobility Particle Sizer (TSI Inc.) were converted to mass concentration using an assumed density of 1.4 g cm^{-3}, and converted to carbon concentration via AMS-measured O:C and H:C ratios.[61] pOC is characterized by average properties of TD-AMS volatility bins. Particle-phase composition was also measured by the I^- CIMS using a "FIGAERO" inlet. Due to decomposition during thermal desorption, this instrument is also limited to characterization of pOC by average properties, which are found to be similar to measurements by AMS in concentration, elemental composition, carbon number, and volatility. All pOC data shown in Figs. 1-4 are consequently from TD-AMS, as it has higher time resolution and lower uncertainty.[62] Further detail on pOC composition is discussed in Supplementary Sects. 2 and 4. Calibration and data analysis was performed where possible through previously published techniques and with commercially available software. Detailed information regarding the comprehensive calibration of I^- CIMS data, and identification and quantification of species in PTR-MS data are described in Supplementary Information Sects. 2 and 3.

Calculation of chemical parameters

Gas-phase mass spectrometers measure individual ions with a known molecular formula, while the TD-AMS provides bulk measurements of chemical properties. To explore chemical evolution, volatility is inferred from molecular composition and vice-versa based on the approach of Daumit et al.[31] that relates c^* to n_C and elemental ratios (e.g. those measured by the AMS). $\overline{\mathrm{OS_C}}$ is calculated from elemental ratios.[42]

Lifetime against atmospheric oxidation for a compound, *i*, is calculated from its rate constant for reaction with OH as $\tau_{ox,i} = \left(k_{OH,i}\overline{[\mathrm{OH}]}\right)^{-1}$ assuming an average OH concentration of 2×10^6 molec cm^{-3}: OH rate constants for known compounds (those labeled in Figs. 1 and 2) are obtained from the NIST Chemical Kinetics Database.[44] Rate constants for unidentified ions are calculated from molecular formula as described by Donahue and co-workers,[45] which spans an atmospheric lifetime of 13 hours for small (high-volatility) gases to ~2 hours for larger, lower volatility (e.g., IVOC) gases. Lifetime of unmeasured mass is estimated from its time dependence (~4 hours, Supplementary Fig. 9). Carbon is assumed to be lost from the particle phase with a lifetime of 69 days, as determined by Kroll and co-workers;[46] the conclusions in this work are insensitive to uncertainties in this value.

Uncertainty in carbon closure

Most uncertainties in all instrument calibrations introduce random error, not bias. Total uncertainty is consequently calculated by adding in quadrature the absolute uncertainty in each ion concentration. Relative uncertainty in total measured carbon is thus lower than the relative uncertainty of any given ion. Instrument, and total uncertainties are provided in Supplementary Tables 1 and 2. The largest source of uncertainty in the total measured concentration is in the calibration of the I^- CIMS, which in this work is ~60% for its total carbon concentration (see Supplementary Sect. 4), though expected to be reduced to 20% in future work. The other main source of uncertainty in this work is the predicted bias in PTR measurements caused by the loss of carbon as neutral fragments in the mass spectrometer. Spectra of oxygenated and non-oxygenated compounds previously published and measured as part of this work

demonstrate that compounds containing more than a few carbon atoms can lose 20% of their carbon as neutral fragments leading to potential underestimation and asymmetry in uncertainty estimates (see Supplementary Sect. 3). Fragmentation during analysis is also expected to somewhat bias the chemical characterization of the product mixture toward ions with lower carbon numbers. This bias cannot explain the observed decrease in n_C, as this trend is also observed in the I^- CIMS, which does not undergo increased fragmentation of more oxidized ions. The contribution of each instrument to total uncertainty in measured carbon is weighted by the fraction of carbon measured, which mitigates the relatively high uncertainty in I^- CIMS calibration due to its minority contribution to total measured carbon. The uncertainty in total carbon contributed by each instrument is: ±16% from I^- CIMS, ±1% from NO_3^- CIMS, $^{+11}_{-7}$% from PTR-MS, ±1% from TILDAS, and ±3% from AMS/SMPS. Overall uncertainty in total measured carbon is ±20%; details provided in Supplementary Table 1.

Carbon closure is not substantially impacted by overlap between carbon measured by multiple instruments. The estimated overlap is 20 ppbC, which accounts for known possible transformations in instruments (e.g. dehydration in the PTR-MS). Though not all possible transformations are well known or constrained, this estimate of multiply-measured carbon is likely an overestimate in that it does not consider time-dependence of ions; even ions measured by multiple instruments that do not correlate, which would represent different isomers, are included in the reported overlap.

Gas-particle-wall partitioning

Deposition of vapors to the walls was modeled as equilibrium gas-particle-wall partitioning of the observed carbon volatility distribution using parameters to match the conditions of these experiments, using a similar approach to that of La and coworkers.[63] Briefly, the fraction of a volatility bin expected to be on the wall was modeled as a function of equilibration time, with parameterized competition between gas-wall partitioning, gas-particle partitioning, and reaction with OH to form a gas-phase product that does not partition. Time evolution of carbon on walls was simulated by modeled phase partitioning of the observed time-evolving volatility distribution of carbon. Details of these calculations are provided in Supplementary Sect. 4.

Data Availability

A list of all ions measured in this work are provided in online as Supplementary Data 1. Time-resolved concentrations of all ions throughout the photooxidation and ozonolysis experiments (shown in Figures 1 and 2, forming the basis for Figures 3 and 4) are available by contacting the corresponding authors.

References

1. Sillman, S. The relation between ozone, NO_x and hydrocarbons in urban and polluted rural environments. *Atmos. Environ.* **33,** 1821–1845 (1999).

2. Atkinson, R. Atmospheric chemistry of VOCs and NO_x. *Atmos. Environ.* **34,** 2063–2101 (2000).

3. Lelieveld, J., Gromov, S., Pozzer, A. & Taraborrelli, D. Global tropospheric hydroxyl distribution, budget and reactivity. *Atmos. Chem. Phys.* **16,** 12477–12493 (2016).

4. Yang, Y. *et al.* Towards a quantitative understanding of total OH reactivity: A review. *Atmos. Environ.* **134,** 147–161 (2016).

5. Zhang, Q. *et al.* Ubiquity and dominance of oxygenated species in organic aerosols in anthropogenically-influenced Northern Hemisphere midlatitudes. *Geophys. Res. Lett.* **34,** 1–6 (2007).

6. Jimenez, J.-L. *et al.* Evolution of Organic Aerosols in the Atmosphere. *Science* **326,** 1525–1529 (2009).

7. Aumont, B., Szopa, S. & Madronich, S. Modelling the evolution of organic carbon during its gas-phase tropospheric oxidation: development of an explicit model based on a self generating approach. *Atmos. Chem. Phys.* **5,** 24975–2517 (2005).

8. Kroll, J. H. & Seinfeld, J. H. Chemistry of secondary organic aerosol: Formation and evolution of low-volatility organics in the atmosphere. *Atmos. Environ.* **42,** 3593–3624 (2008).

9. Cappa, C. D. & Wilson, K. R. Multi-generation gas-phase oxidation, equilibrium partitioning, and the formation and evolution of secondary organic aerosol. *Atmos. Chem. Phys.* **12,** 9505–9528 (2012).

10. Donahue, N. M., Epstein, S. A., Pandis, S. N. & Robinson, A. L. A two-dimensional volatility basis set: 1. organic-aerosol mixing thermodynamics. *Atmos. Chem. Phys.* **11,** 3303–3318 (2011).

11. Goldstein, A. H. & Galbally, I. Known and Unexplored Organic Constituents in the Earth's Atmosphere. *Environ. Sci. Technol.* **41,** 1514–1521 (2007).

12. Calvert, J. G., Derwent, R. G., Orlando, J. J., Tyndall, G. S. & Wallington, T. J. *Mechanisms of Atmospheric Oxidation of the Alkanes*. (Oxford University Press, 2007).

13. Lee, A. *et al.* Gas-phase products and secondary aerosol yields from the photooxidation of 16 different terpenes. *J. Geophys. Res. Atmos.* **111,** D17305 (2006).

14. Lee, A. *et al.* Gas-phase products and secondary aerosol yields from the ozonolysis of ten different terpenes. *J. Geophys. Res. Atmos.* **111,** D07302 (2006).

15. Zhang, X. *et al.* Influence of vapor wall loss in laboratory chambers on yields of secondary organic aerosol. *Proc. Natl. Acad. Sci. U. S. A.* **111,** 5802–5807 (2014).

16. Robinson, A. L. *et al.* Rethinking Organic Aerosols: Semivolatile Emissions and Photochemical Aging. *Science* **315,** 1259–1262 (2007).

17. Isaacman-VanWertz, G. *et al.* Using advanced mass spectrometry techniques to fully characterize atmospheric organic carbon: current capabilities and remaining gaps. *Faraday Discuss.* **200,** 579–598 (2017).

18. Decarlo, P. F. *et al.* Field-Deployable, High-Resolution, Time-of-Flight Aerosol Mass Spectrometer. *Anal. Chem.* **78,** 8281–8289 (2006).

19. Graus, M., Müller, M. & Hansel, A. High resolution PTR-TOF: Quantification and Formula Confirmation of VOC in Real Time. *J. Am. Soc. Mass Spectrom.* **21,** 1037–1044 (2010).

20. Jordan, A. *et al.* A high resolution and high sensitivity proton-transfer-reaction time-of-flight mass spectrometer (PTR-TOF-MS). *Int. J. Mass Spectrom.* **286,** 122–128 (2009).

21. Aljawhary, D., Lee, A. K. Y. & Abbatt, J. P. D. High-resolution chemical ionization mass spectrometry (ToF-CIMS): Application to study SOA composition and processing. *Atmos. Meas.*

405 *Tech.* **6,** 3211–3224 (2013).

406 22. Jokinen, T. *et al.* Atmospheric sulphuric acid and neutral cluster measurements using CI-APi-TOF.
407 *Atmos. Chem. Phys.* **12,** 4117–4125 (2012).

408 23. Krechmer, J. E. *et al.* Formation of Low Volatility Organic Compounds and Secondary Organic
409 Aerosol from Isoprene Hydroxyhydroperoxide Low-NO Oxidation. *Environ. Sci. Technol.* **49,**
410 10330–10339 (2015).

411 24. Lee, B. H. *et al.* An Iodide-Adduct High-Resolution Time-of-Flight Chemical- Ionization Mass
412 Spectrometer: Application to Atmospheric Inorganic and Organic Compounds. *Environ. Sci.*
413 *Technol.* **48,** 6309–6317 (2014).

414 25. Lopez-Hilfiker, F. D. *et al.* Constraining the sensitivity of iodide adduct chemical ionization mass
415 spectrometry to multifunctional organic molecules using the collision limit and thermodynamic
416 stability of iodide ion adducts. *Atmos. Meas. Tech.* **9,** 1505–1512 (2016).

417 26. Eddingsaas, N. C. *et al.* α-pinene photooxidation under controlled chemical conditions-Part 1:
418 gas-phase composition in low-and high-NO x environments. *Atmos. Chem. Phys.* **12,** 6489–6504
419 (2012).

420 27. Capouet, M., Peeters, J., Nozière, B. & Müller, J.-F. Alpha-pinene oxidation by OH: simulations of
421 laboratory experiments. *Atmos. Chem. Phys. Discuss.* **4,** 4039–4103 (2004).

422 28. Pathak, R. K., Stanier, C. O., Donahue, N. M. & Pandis, S. N. Ozonolysis of a-pinene at
423 atmospherically relevant concentrations: Temperature dependence of aerosol mass fractions
424 (yields). *J. Geophys. Res. Atmos.* **112,** D03201 (2007).

425 29. Donahue, N. M. *et al.* Aging of biogenic secondary organic aerosol via gas-phase OH radical
426 reactions. *Proc. Natl. Acad. Sci. U. S. A.* **109,** 13503–13508 (2012).

427 30. Hatakeyama, S., Ohno, M., Weng, J., Takagi, H. & Akimoto, H. Mechanism for the formation of
428 gaseous and particulate products from ozone-cycloalkene reactions in air. *Environ. Sci. Technol.*
429 **21,** 52–57 (1987).

430 31. Daumit, K. E., Kessler, S. H. & Kroll, J. H. Average chemical properties and potential formation
431 pathways of highly oxidized organic aerosol. *Faraday Discuss.* **165,** 181–202 (2013).

432 32. Ehn, M. *et al.* A large source of low-volatility secondary organic aerosol. *Nature* **506,** 476–479
433 (2014).

434 33. Ehn, M. *et al.* Composition and temporal behavior of ambient ions in the boreal forest. *Atmos.*
435 *Chem. Phys.* **10,** 8513–8530 (2010).

436 34. Saunders, S. M., Jenkin, M. E., Derwent, R. G. & Pilling, M. J. Protocol for the development of the
437 Master Chemical Mechanism, MCM v3 (Part A): tropospheric degradation of non-aromatic
438 volatile organic compounds. *Atmos. Chem. Phys.* **3,** 161–180 (2003).

439 35. Worton, D. R., Gentner, D. R., Isaacman, G. & Goldstein, A. H. Embracing complexity: Deciphering
440 origins and transformations of atmospheric organics through speciated measurements. *Environ.*
441 *Sci. Technol.* **46,** 5265–5266 (2012).

442 36. Nah, T. *et al.* Influence of seed aerosol surface area and oxidation rate on vapor wall deposition
443 and SOA mass yields: A case study with α-pinene ozonolysis. *Atmos. Chem. Phys.* **16,** 9361–9379

(2016).

37. Trump, E. R., Epstein, S. A., Riipinen, I. & Donahue, N. M. Wall effects in smog chamber experiments: A model study. *Aerosol Sci. Technol.* **50,** 1180–1200 (2016).

38. Ye, P. *et al.* Vapor wall loss of semi-volatile organic compounds in a Teflon chamber. *Aerosol Sci. Technol.* **50,** 822–834 (2016).

39. Nozière, B., Barnes, I. & Becker, K.-H. Product study and mechanisms of the reactions of α-pinene and of pinonaldehyde with OH radicals. *J. Geophys. Res. Atmos.* **104,** 23645–23656 (1999).

40. Iyer, S., Lopez-Hilfiker, F. D., Lee, B. H., Thornton, J. A. & Kurtén, T. Modeling the Detection of Organic and Inorganic Compounds Using Iodide-Based Chemical Ionization. *J. Phys. Chem. A* **120,** 576–587 (2016).

41. Pagonis, D., Krechmer, J. E., Gouw, J. De, Jimenez, J. L. & Ziemann, P. J. Effects of gas – wall partitioning in Teflon tubing and instrumentation on time-resolved measurements of gas-phase organic compounds. *Atmos. Meas. Tech.* 4687–4696 (2017).

42. Kroll, J. H. *et al.* Carbon oxidation state as a metric for describing the chemistry of atmospheric organic aerosol. *Nat. Chem.* **3,** 133–139 (2011).

43. Lee, B. H. *et al.* Highly functionalized organic nitrates in the southeast United States: Contribution to secondary organic aerosol and reactive nitrogen budgets. *Proc. Natl. Acad. Sci. U. S. A.* **113,** 1516–1521 (2016).

44. Manion, J. A. *et al. NIST Chemical Kinetics Database, NIST Standard Reference Database 17, Version 7.0 (Web Version), Release 1.6.8, Data version 2015.12*. (National Institute of Standards and Technology, 2015).

45. Donahue, N. M. *et al.* Why do organic aerosols exist? Understanding aerosol lifetimes using the two-dimensional volatility basis set. *Environ. Chem.* **10,** 151–157 (2013).

46. Kroll, J. H., Lim, C. Y., Kessler, S. H. & Wilson, K. R. Heterogeneous Oxidation of Atmospheric Organic Aerosol: Kinetics of Changes to the Amount and Oxidation State of Particle-Phase Organic Carbon. *J. Phys. Chem. A* **119,** 10767–10783 (2015).

47. Dixon-Lewis, G. Flames Structure and Flame Reaction Kinetics VII. Reactions of Traces of Heavy Water, Deuterium and Carbon Dioxide added to rich Hydrogen + Nitrogen + Oxygen Flames. *Proc. R. Soc. London A* **330,** 219–245 (1972).

48. Raff, J. D., Stevens, P. S. & Hites, R. A. Relative rate and product studies of the OH - Acetone reaction. *J. Phys. Chem. A* **108,** 4728–4735 (2005).

49. Richards-henderson, N. K., Goldstein, A. H. & Wilson, K. R. Large Enhancement in the Heterogeneous Oxidation Rate of Organic Aerosols by Hydroxyl Radicals in the Presence of Nitric Oxide. *J. Phys. Chem. Lett.* **6,** 4451–4455 (2015).

50. Paulot, F. *et al.* Unexpected Epoxide Formation in the Gas-Phase Photooxidation of Isoprene. *Science* **325,** 730–733 (2013).

51. Surratt, J. D. *et al.* Reactive intermediates revealed in secondary organic aerosol formation from isoprene. *Proc. Natl. Acad. Sci.* **107,** 6640–6645 (2010).

52. Palm, B. B. *et al.* In situ secondary organic aerosol formation from ambient pine forest air using an oxidation flow reactor. *Atmos. Chem. Phys.* **16,** 2943–2970 (2016).

53. Chan, A. W. H. *et al.* Speciated measurements of semivolatile and intermediate volatility organic compounds (S/IVOCs) in a pine forest during BEACHON-RoMBAS 2011. *Atmos. Chem. Phys.* **16,** 1187–1205 (2016).

54. Tkacik, D. S., Presto, A. A., Donahue, N. M. & Robinson, A. L. Secondary organic aerosol formation from intermediate-volatility organic compounds: Cyclic, linear, and branched alkanes. *Environ. Sci. Technol.* **46,** 8773–8781 (2012).

55. Park, J.-H. *et al.* Active Atmosphere-Ecosystem Exchange of the Vast Majority of Detected Volatile Organic Compounds. *Science* **341,** 643–648 (2013).

56. Nguyen, T. B. *et al.* Rapid deposition of oxidized biogenic compounds to a temperate forest. *Proc. Natl. Acad. Sci. U. S. A.* **112,** E392-401 (2015).

57. Wolfe, G. M. *et al.* Formaldehyde production from isoprene oxidation across NOx regimes. *Atmos. Chem. Phys.* **16,** 2597–2610 (2016).

58. Warneke, C. *et al.* Photochemical aging of volatile organic compounds in the Los Angeles basin: Weekday-weekend effect. *J. Geophys. Res. Atmos.* **118,** 5018–5028 (2013).

59. Faulhaber, A. E. *et al.* Characterization of a thermodenuder-particle beam mass spectrometer system for the study of organic aerosol volatility and composition. *Atmos. Meas. Tech.* **2,** 15–31 (2009).

60. McManus, J. B. *et al.* Pulsed quantum cascade laser instrument with compact design for rapid, high sensitivity measurements of trace gases in air. *Appl. Phys. B Lasers Opt.* **92,** 387–392 (2008).

61. Canagaratna, M. R. *et al.* Elemental ratio measurements of organic compounds using aerosol mass spectrometry: Characterization, improved calibration, and implications. *Atmos. Chem. Phys.* **15,** 253–272 (2015).

62. Lopez-Hilfiker, F. D. *et al.* A novel method for online analysis of gas and particle composition: Description and evaluation of a filter inlet for gases and AEROsols (FIGAERO). *Atmos. Meas. Tech.* **7,** 983–1001 (2014).

63. La, Y. S. *et al.* Impact of chamber wall loss of gaseous organic compounds on secondary organic aerosol formation: Explicit modeling of SOA formation from alkane and alkene oxidation. *Atmos. Chem. Phys.* **16,** 1417–1431 (2016).

Acknowledgements

We would like to thank Harald Stark for insights into correcting for mass-dependent transmission in the I^- CIMS calibration, Jose-Luis Jimenez for valuable discussions regarding vapor wall loss, Colette Heald for valuable discussions of overall chemical trends, and Laura Wattenberg for the inspiration for the stacked plot approach to visualizing these data. This work was supported in part by the NSF Postdoctoral Research Fellowship program (AGS-PRF 1433432), as well as grants AGS-1536939, AGS-1537446 and AGS- 1536551. D. A. Knopf acknowledges support from NSF grant AGS-1446286.

Author Contribution

Experiments were conducted by GIVW, PM, REO, CL, JBN, JPF, PKM, CA, LS, DAK, ATL, JRR, and STH, with data analysis by these researchers with significant contributions by JAM, JFH, AHG, TBO, MRC, JHK, JTJ, DRW. GIVW and JHK interpreted the results. This manuscript was prepared by GIVW and JHK, with contributions and editing by all listed authors.

Competing Financial Interests

PM, JBN, JRR, STH, TBO, MRC, JTJ, and DRW are, or were during this work, employees of Aerodyne Research, Inc. (ARI), which developed and commercialized several of the advanced mass spectrometric instruments utilized in this study.

Materials & Correspondence

All correspondence should be addressed to Prof. Gabriel Isaacman-VanWertz at ivw@vt.edu or Prof. Jesse Kroll at jhkroll@mit.edu .

Figure 1. Measured carbon in the photooxidation of α-pinene, characterized by molecular formula. Each product ion of α-pinene (dark gray) is colored by the instrument by which it was measured (green: AMS/SMPS, purple: PTR-MS, light gray: TILDAS, orange: I^- CIMS). Unlabeled species measured by TILDAS are formic acid and formaldehyde. Uncertainty range for each instrument shown on right. Carbon closure is achieved within measurement uncertainty (102±20%) with expected carbon in the system (light gray dashed line at ~550 ppbC, which accounts for dilution of the precursor), providing an unprecedented opportunity to study the complete chemical evolution of atmospheric oxidation processes. All concentrations are corrected for dilution; pOC is also corrected for particle deposition to the chamber walls. Bottom panel: modeled OH concentration (red line) and approximate photochemical age in the atmosphere (blue dashed line), assuming an average atmospheric OH concentration of 2×10^6 molec cm^{-3}. The corresponding plot for the α-pinene ozonolysis experiment is given in Supplementary Fig. 6.

Figure 2. Chemical characterization of carbon measured in the photooxidation of α-pinene in terms of $\overline{OS_C}$ and *c**, commonly used for simplified representation of atmospheric organic carbon. These measurements illustrate the highly dynamic nature of the chemical system. Circle area is proportional to carbon concentration. Hollow: α-pinene, light gray: gas-phase species, dark gray: pOC, shown at average $\overline{OS_C}$ of each volatility bin measured by TD-AMS. Gas-phase species containing nitrate groups (defined as containing nitrogen and ≥3 oxygen atoms) are outlined. Distributions are provided after approximately (**a**) 1 hour, (**b**) 4 hours, and (**c**) 24 hours of equivalent atmospheric age. Some products are observed to increase in concentration throughout the experiment (e.g., CO), while others form and are then depleted (e.g., pinonaldehyde), demonstrating differences in reactivity and lifetime drive the dominant formation of less-reactive products. The full time evolution of these data is available as online as Supplementary Videos 1 and 2.

Figure 3. Distribution of key chemical properties of gas- and particle-phase products during the photooxidation of a-pinene: (**a**) number of carbon atoms, n_C, (**b**) oxidation state of carbon, $\overline{OS_C}$, and (**c**) volatility in terms of saturation concentration, c^*, each denoted by the color scale shown. The properties of only the measured oxidation products (and not of the α-pinene precursor or the "unmeasured" carbon) are shown; the plots in which α-pinene is included is provided in Supplementary Fig. 6. Evolution of distributions and carbon-weighted averages of each property (bottom panels) demonstrate several general trends in atmospheric oxidation: initial formation of pOC and lightly-oxygenated moderately-volatile products, followed by fragmentation of gases to yield small oxygenated compounds.

Figure 4. Changes in atmospheric lifetime and reactivity through multigenerational oxidation of a-pinene. (**a**) Time-dependent distribution of atmospheric lifetime against oxidation by OH (τ_{ox}) including unmeasured carbon (for which assumed τ_{ox} = 4 h). Average trend shown in bottom panel. (**b**) The volatility distribution of carbon at two points in the experiment. Times shown are denoted by arrows in panel (a): relatively early (top) and late (bottom) in the reaction. Volatility bins are colored by τ_{ox} with the same color scale as in panel a. Unmeasured carbon is assumed to be distributed evenly across c^*= 10^2-10^4 μg m^{-3} (hashed bars) for illustrative purposes. (**c**) Carbon-weighted average OH reactivity (assuming average OH concentration of 2×10^6 molec cm^{-3}). Exponential fit (black dashed line) has a decay constant, $\tau_{\overline{k_{OH}}}$, of 2.8 hours. The average observed trend of increasing lifetime is shown to lead to the sequestration of carbon into high- and low-volatility reservoirs of low-reactivity carbon (small oxygenated gases and pOC, respectively) and a rapid decrease in overall reactivity.

Supplementary Information: Chemical evolution of atmospheric organic carbon over multiple generations of oxidation

Gabriel Isaacman-VanWertz[1,2]*, Paola Massoli[3], Rachel O'Brien[1], Christopher Lim[1], Jonathan P. Franklin[1], Joshua A. Moss[1], James F. Hunter[1], John B. Nowak[3,#], Manjula R. Canagaratna[3], Pawel K. Misztal[4], Caleb Arata[4], Joseph R. Roscioli[3], Scott T. Herndon[3], Timothy B. Onasch[3], Andrew T. Lambe[3], John T. Jayne[3], Luping Su[5], Daniel A. Knopf[5], Allen H. Goldstein[4], Douglas R. Worsnop[3], Jesse H. Kroll[1]*

[1]Department of Civil and Environmental Engineering, Massachusetts Institute of Technology, Cambridge, Massachusetts 02139, USA

[2]Department of Civil and Environmental Engineering, Virginia Tech, Blacksburg, Virginia 24061, USA

[3]Aerodyne Research Inc., Billerica, Massachusetts 01821, USA

[4]Department of Environmental Science, Policy, and Management, University of California, Berkeley, California 94720, USA

[5]School of Marine and Atmospheric Sciences, Stony Brook University, Stony Brook, New York 11794, USA

[#]Now at NASA Langley Research Center, Hampton, VA 23681, USA

This Supplementary Information contains:

1. Instrumentation and uncertainty

1.1. Operating conditions

Reaction chamber

A 7.5 m^3 fixed-volume Teflon environmental chamber (Ingeniven LLC) was filled with clean air generated on site (Aadco 737-13 Pure Air Generator). Seed aerosol was introduced by atomizing a 1 g L^{-1} solution of ammonium sulfate (TSI Aerosol Generator 3076) and sending the resulting particles to the chamber through a dryer and Po-210 static eliminator (NRD LLC). Liquid injection was used to introduce both the pure precursor compound and a hexafluorobenzene, a non-reactive tracer used to measure dilution rate (both >99% purity, Sigma-Aldrich). After allowing 20 minutes for mixing, oxidant or oxidant precursor was added. For ozonolysis, approximately 350 ppb ozone was added using an ozone generator (Model 600, Jelight Company Inc.) supplied with pure O_2 (4.9, Airgas). For photooxidation, HONO was generated in-situ through addition of H_2SO_4 (1 M) to a $NaNO_3$ (1 M). After all reagents were allowed to mix, the ultraviolet lights were turned on to initiate reaction; lights have a typical blacklight spectrum (maximum emission at ~350 nm) and an intensity that yields a value for J_{NO2} of 0.06-0.08 min^{-1}. All experiments were performed at 20 °C and very low relative humidity (<5%). Additional detail regarding general operation of this chamber is reported by Hunter et al.[1] OH concentrations were estimated using the F0AM model.[2]

The reaction chamber was maintained at slight positive pressure (20-40 mbar) through the addition of clean air to compensate for instrument sampling. A constant dilution flow of 10 lpm was supplied, leading to an expected dilution rate of ~2×10^{-5} s^{-1}, in agreement with that determined from tracer concentrations. The wall loss rate of seed particles prior to reaction was confirmed by the loss rate of particles at the end of the experiment when the organic-to-sulfate ratio is stable (indicating no production of particles). Particle loss rate was 8×10^{-5} s^{-1} during photoxidation and 5×10^{-5} s^{-1} during ozonolysis.

All high-resolution time-of-flight mass spectrometers used in this work (I^- CIMS, PTR-MS, NO_3^- CIMS, TD-AMS) have a mass resolution of m/Δm = ~4000. This resolution is insufficient for unambiguous identification of all molecular formulas. However, in a system limited to organic elements (C, H, O, N, S), the mass defect is inherently correlated with chemical properties such as $\overline{OS_C}$.[3] Consequently, random errors in formula attribution will not substantially impact distributions and trends in chemical properties.

I^- CIMS

An "I^- CIMS" (Aerodyne Research Inc.) was used to measure analytes by reacting them with I^- generated by the ionization of methyl iodide, accessing a wide range of oxidized compounds.[4,5] The chamber is sampled at 1 lpm. For direct measurement of gases, sample flow is diluted by 9 lpm for a total flow of 10 lpm through a ¼" O.D. Teflon sample line to minimize residence time and thus loss within the inlet. A subsample of 2 lpm of this flow enters the ionization region of the instrument for analysis. Particle-phase measurements were collected using a Filter Inlet for Gases and AEROsols ("FIGAERO"),[6,7] with one sample every 15 minutes. Particles were concentrated on a 2µm PTFE filter with PTFE support (Zefluor™ Membrane, Pall Corporation) for 5 minutes at 1 lpm, then thermally desorbed into the instrument in a 2 slpm stream of nitrogen heated with a temperature ramp up to 200 °C. Data analysis was performed in Igor Pro 6.3 (Wavemetrics, Inc.) using the commercially available package Tofware 2.5.6.

For calibration, we apply the general approach outlined by Lee et al., Iyer et al., and Lopez-Hilfiker et al. to account for differences in sensitivity caused by the varying strengths of the analyte-iodide cluster.[4,5,8] This approach has not previously been comprehensively applied to a large suite of unknown compounds, so a detailed discussion (including a discussion of uncertainty) is provided below (Section S2). Initial reaction is generally expected to occur through clustering with I^-, so only ions containing iodide are considered in this analysis. Calibration was validated in part by comparing composition measured by I^- CIMS using the FIGAERO inlet to that measured by AMS (Supplementary Figure 4).

PTR-MS

Gas-phase compounds, in particular volatile and lightly oxidized gases, were measured with a Proton Transfer Reaction-Mass Spectrometer (Ionikon Analytik) by reacting analytes with H_3O^+ to produce ions of molecular formula plus H^+.[9,10] Sample was collected at 200 sccm through a Teflon filter (2 µm pore diameter) and a 1 meter line heated to only 80 °C, so quantitative measurement is limited to compounds of relatively high volatility. Data analysis was performed using PTRwid v2[11] run in Interactive Data Language (IDL). Calibration was performed using authentic standards to estimate a general response factor with a molecular-weight-based transmission factor adjustment, as discussed in detail elsewhere.[12–14] Exceptions to this generalized calibration approach are ions representing compounds to which explicit chemical identities have been assigned in the main text (α-pinene, acetic acid, acetone, and pinonaldehyde). Calibration of these "identified ions" is discussed in detail in Supplementary Sect. 3. Uncertainty for ions representing known compounds is estimated at ±15%, while uncertainty for unknown ions is -10%/+30%, which is asymmetric due to loss of neutral fragments leading to underestimation of carbon (see below). Concentrations of ions CH_2OH^+ and $CH_2O_2H^+$, representing formaldehyde and formic acid, respectively, are not included in PTR-MS data as they are measured independently and with more selectivity and accuracy by the TILDAS.

NO_3^- CIMS

A "NO_3^- CIMS" (Aerodyne Research Inc.) was used to measure low-volatility, highly-oxidized gases by clustering them with NO_3^- generated by the x-ray ionization of nitric acid.[15,16] Analytes are transported to the ionization region at 10 lpm, with 1 lpm sampled from the chamber and 9 lpm of introduced nitrogen sheath flow. Ionization of analytes occurs in the centerline of flow and little or no loss to surfaces are expected due to the inlet design.[17] A portion of the centerline flow (0.8 lpm) is sampled into the instrument for analysis. Data analysis was performed in Igor Pro 6.3 (Wavemetrics, Inc.) using the commercially available package Tofware version 2.5.6, following the practices described by Stark et al.[3] Calibration is performed by measuring the kinetically-limited reaction rate using malonic acid[18] and assuming all ions react with the reagent ion at this rate. Reported concentrations therefore represent a lower-limit concentration of these species. Given the very low concentrations of these compounds, even significant underestimation of these compounds would not substantially impact the conclusions of this work. Concentrations measured in this work are comparable to previously reported concentrations of these compounds.[19] As discussed below, NO_3^- CIMS measured <1% of total carbon under photooxidation conditions. Contribution from NO_3^- CIMS to uncertainty in overall total carbon measured is 1%.

TD-AMS

Ensemble particle composition was measured using an Aerodyne Aerosol Mass Spectrometer ("AMS"; Aerodyne Research Inc.)[20] operated downstream of a Thermal Denuder, which measures the ensemble volatility of the particles.[21] Data analysis was performed in Igor Pro 6.3 (Wavemetrics, Inc.) using the commercially available packages PIKA v1.16 and SQUIRREL v1.57.[22] Elemental composition of the organic fraction was calculated within each volatility bin based on the molecular formulas of the fragments using the updated approach of Canagaratna et al.[23] Particle mass concentrations were measured by a Scanning Mobility Particle Sizer ("SMPS", TSI Inc.) using an assumed density of 1.4 μg m^{-3} for α-pinene derived organic particles,[24] and a known density of 1.77 μg m^{-3} for ammonium sulfate. The mass concentrations measured by this instrument were coupled with the elemental composition measured by the AMS to quantify particle-phase carbon concentrations in units of ppbC.

The temperature ramp of the Thermal Denuder was cycle from 40 °C to 190 °C and back down again in 45 minutes. A continuously evolving volatility estimate in terms of mass fraction remaining at a given temperature is then turned into an approximate volatility distribution. Operating conditions instrument were similar to that of Faulhaber et al.,[21] so the same conversion between temperature and volatility bin is applied. Uncertainty in the volatility distribution does not impact any of the conclusions in this work, as the vapor wall loss modeling is only very weakly sensitive to the particle-phase volatility distribution.

TILDAS

Compounds containing one carbon atom were measured by Tunable Infrared Laser Differential Absorption Spectrometers (TILDAS, Aerodyne Research Inc.), [25] detecting high-resolution infrared absorptions at 1764.90 cm^{-1} for formaldehyde, 1765.025 cm^{-1} for formic acid, and 2199.93 cm^{-1} for CO. Formic acid and formaldehyde were measured on one instrument while CO was measured on a separate instrument. Zero air was automatically sampled every 15 minutes to ensure proper background subtraction. Uncertainty is estimated to be ±15% for formaldehyde and formic acid, and <5% for CO. Data was analyzed by fitting the observed absorption spectra to lines in the HITRAN database.[26] Calibration of formaldehyde and formic acid is based upon the known linestrengths of the molecules. The CO measurement is referenced to an authentic standard every few weeks (for which the calibration value is between 0.98 and 1.02).

1.2. Uncertainty

In Supplementary Tables 1 and 2 we provide an overview of uncertainty in each instrument and the contribution of each instrument to total uncertainty for photooxidation and ozonolysis. Uncertainties reported in these tables for I^- CIMS and PTR-MS are discussed in detail below; uncertainties for the other instruments are from the cited literature. For most instruments, the dominant source of uncertainty is error in the calibration, uncertainty in instrument operating conditions (e.g. flow rates), and uncertainty in applied assumptions (e.g. density of pOC, loss of neutral carbon in PTR-MS discussed below). The I^- and NO_3^- CIMS uncertainty is dominated by variability and uncertainty in ion sensitivities, which is discussed in detail below. Most errors are uncorrelated, including uncertainty in the sensitivity of any given ion or uncertainty of different instruments, so summed uncertainty for these errors is estimated as the quadrature addition of each absolute uncertainty, i.e. the square root of the sum of the squares. Consequently, the relative uncertainty in the total carbon measured by any one instrument is substantially lower than that for any given ion. Uncertainty in the identified and unidentified ions

measured by the PTR-MS are at least partly correlated (that is, both dependent on uncertainty in PTR-MS parameters and operating conditions), so these errors are added linearly. Uncertainty in the total measured carbon of all instruments is estimated as the quadrature addition of the uncertainties in each instrument as noted in footnote *c* of Supplementary Table 1. Overall total uncertainty is found here to be -18/+20% (1σ); we therefore report total uncertainty in this work as ±20%.

Supplementary Table 1. Contributions to measured carbon and uncertainty for photooxidation experiment.

	Measured ppbC	Percentage of total measured	Uncertainty per species[a]	Dominant source of uncertainty	Uncertainty in total measured per instrument				Uncertainty in overall total measured	
					-/+ %		-/+ ppbC		-/+ %	
	C_i	$\frac{C_i}{\sum_i C_i}$			σ_i		Δ_i		$\frac{\Delta_i}{\sum_i C_i}$	
Photooxidation										
PTR - identified	191	34%	<15%	*1*	-15%	15%	-29	29	-5%	5%
PTR - unidentified	107	19%	30%	*1,2,3*	-10%	30%	-11	32	-2%	6%
(Total PTR)	*298*	*52%*					*-40*[b]	*61*[b]	*-7%*	*11%*
AMS/SMPS	77	14%	*n/a*	*1,4*	-20%	20%	-15	15	-3%	3%
TILDAS	40	7%	<15%	*1*	-15%	15%	-6	6	-1%	1%
I^- CIMS	155	27%	2.5x	*5*	-60%	60%	-93	93	-16%	16%
NO_3^- CIMS[e]	2	0.4%	unknown	*1,4*	-200%	200%	-4	4	-0.7%	0.7%
Total measured	**572**						**103**[c]	**112**[c]	**18%**[d]	**20%**[d]

Sources of uncertainty: 1 - calibration error; 2 - instrumentation operating parameters (e.g., uncertainties in flows); 3 - neutral loss of carbon, leads to asymmetry in total uncertainty; 4 - density assumption; 5 - individual ion sensitivities

[a] Species measured by TILDAS are compounds, all others are ions; AMS/SMPS measures only bulk, not per species

[b] uncertainty in identified and unidentified ions not entirely uncorrelated, so added directly, not in quadrature. Conservative estimate as some fraction of these uncertainties are uncorrelated

[c] absolute total uncertainty is quadrature addition of uncertainties: $\Delta_{tot} = \sqrt{\sum_i \Delta_i^2} = \sqrt{\sum\left(\Delta_{total\ PTR}^2 + \Delta_{I^-\ CIMS}^2 + \Delta_{TILDAS}^2 + \Delta_{AMS/SMPS}^2\right)}$

[d] relative total uncertainty is absolute total uncertainty as a fraction of total measured mass: $\sigma_{tot} = \frac{\Delta_{tot}}{\sum_i C_i}$

[e] uncertainty not well constrained. High values used to demonstrate insensitivity of total uncertainty to this term

Supplementary Table 2. Contributions to measured carbon and uncertainty for ozonolysis experiment.

	Measured ppbC	Percentage of total measured	Uncertainty per species[a]	Dominant source of uncertainty	Uncertainty in total measured per instrument				Uncertainty in overall total measured	
					-/+ %		-/+ ppbC		-/+ %	
	C_i	$\frac{C_i}{\sum_i C_i}$			σ_i		Δ_i		$\frac{\Delta_i}{\sum_i C_i}$	
Ozonolysis										
PTR - identified	119	31%	<15%	*1*	-15%	15%	-18	18	-5%	5%
PTR - unidentified	135	36%	30%	*1,2,3*	-10%	30%	-14	41	-4%	11%
(Total PTR)	*254*	*67%*					*-32*[b]	*59*[b]	-8%	16%
AMS/SMPS	61	16%	*n/a*	*1,4*	-20%	20%	-12	12	-3%	3%
TILDAS	35	9%	<15%	*1*	-15%	15%	-5	5	-1%	1%
I^- CIMS	30	8%	2.5x	*5*	-60%	60%	-18	18	-5%	5%
Total measured	**380**						**39**[c]	**74**[c]	**10%**[d]	**20%**[d]

Sources of uncertainty: 1 - calibration error; 2 - instrumentation operating parameters (e.g. uncertainties in flows); 3 - neutral loss of carbon, leads to asymmetry in total uncertainty; 4 - density assumption; 5 - individual ion sensitivities

[a] Species measured by TILDAS are compounds, all others are ions; AMS/SMPS measures only bulk, not per species

[b] uncertainty in identified and unidentified ions not entirely uncorrelated, so added directly, not in quadrature. Conservative estimate as some fraction of these uncertainties are uncorrelated

[c] absolute total uncertainty is quadrature addition of absolute uncertainties: $\Delta_{tot} = \sqrt{\sum_i \Delta_i^2}$

[d] relative total uncertainty is absolute total uncertainty as a fraction of total measured mass: $\sigma_{tot} = \frac{\Delta_{tot}}{\sum_i C_i}$

2. Calibration details: I^- CIMS

The response factor of the I^- CIMS to a given analyte is primarily a function of

1. Maximum sensitivity of the instrument, corresponding to the sensitivity to compounds that always cluster with the reagent ion after a collision in the reaction region. Can be estimated theoretically or measured empirically.
2. Strength of the ion-cluster bond, impacting both the formation of the cluster as well as the tendency of the cluster to decompose within the instrument prior to detection. Determines sensitivity relative to the maximum.
3. Mass dependent transmission of ions through the detector, which is a result of loss of ions as a function of molecular weight. Commonly applied correction with time-of-flight mass spectrometers

Each of these factors impacting sensitivity was treated explicitly as discussed below. In many cases, no absolute best correction or calibration could be determined. A Monte Carlo-style calibration was therefore performed, with uncertainty parameterized within reasonable constraints for each of these effects.

2.1. Maximum sensitivity

a. Gas-phase sensitivity

Theoretical sensitivity. Reagent ions interact with sample within the ion-molecule reaction region (IMR), and are assumed to collide at a rate, k_{coll}, of 1×10^{-9} cm^3 $molec^{-1}$ s^{-1}.[27] From this value, for a given operating condition, a theoretical maximum sensitivity can be calculated for compounds for which an analyte-reagent ion cluster forms from each reaction. N_2O_5 has been shown to be one such "kinetically limited" compound, so by measuring this compound, an empirical estimate of maximum sensitivity can be obtained. Lopez-Hilfiker et al.[5] found the empirical and theoretical estimates to be in good agreement, but the instrument used in this work has an IMR with a larger volume, which may decrease empirical sensitivity due to losses to the IMR walls. Consequently, both approaches are explored here.

In theory, concentration of a compound, *X*, in the IMR can be calculated from the observed analyte ion signal (normalized to the primary reagent ion signals), $\frac{i_X}{i_P}$, the collision rate, k_{coll}, and the residence time of the IMR, t_{IMR}, which is calculated from the volumetric flow rate through the IMR volume:

$$[X]_{IMR} = \frac{1}{k_{coll}\, t_{IMR}} \frac{i_X}{i_P} \quad (1)$$

In this work, 2 slpm of flow containing the reagent ions were mixed with 2 slpm of sample flow in an IMR volume of 47 cm^3 at an operating pressure of 200 mbar, so t_{IMR} = 0.13 s. Concentration in the IMR is converted to concentration in the sample flow by:

$$1ppt = 10^{12} \frac{[X]_{samp}}{[M]_{samp}} = 10^{12} \frac{[X]_{IMR}}{[M]_{IMR} * f} \quad (2)$$

where $[M]_{samp}$ is the total concentration of gas molecules in the sample, which constitutes a fraction *f* of the gas molecules in the IMR, $[M]_{IMR}$. In this work, half the flow in the IMR carries the reagent ion and half is sample flow, so *f* = 0.5. By combining equations (1) and (2), an equation for maximum kinetically limited sensitivity, S_{kin}, in units of $i_X\ ppt^{-1} i_P{}^{-1}$ can be formulated:

$$S_{kin} = \frac{\frac{i_X}{i_P}}{ppt} = \frac{[M]_{IMR} f\, k_{coll}\, t_{IMR}}{10^{12}} \quad (3)$$

Using the operating conditions in this work, a theoretical maximum sensitivity is calculated of 300 counts per second per ppt per million reagent ions (µncps ppt^{-1}).

Empirical sensitivity. Known quantities of N_2O_5, to which the I^- CIMS is known to be maximally sensitive, were generated and measured in-situ. High levels of NO_2 (1-2 ppm) were added to the same dry reaction chamber used for oxidation experiments. Under these conditions, N_2O_5 was formed through the addition of small known quantities of ozone:

$$NO_2 + O_3 \rightarrow NO_3 + O_2 \quad (R1)$$

$$NO_3 + NO_2 \leftrightarrow N_2O_5 \quad (R2)$$

Aliquots of ozone were introduced, spanning a range of 1-5 ppb, with each addition allowed to equilibrate until observed signal of the ion $(I)N_2O_5^-$ was stable, approximately 20 minutes. Due to the continuous accumulation of ozone and the effects of dilution and changing equilibrium, concentrations of N_2O_5 at each step were not assumed to be exactly equal to the amount of ozone added, but were rather calculated using the F0AM box model[2] to yield a multi-point calibration. The empirically derived sensitivity for this instrument was observed to be 75 µncps ppt^{-1}.

The theoretical and empirical maximum sensitivities differ by a factor of 4. However, the N_2O_5 calibration was found to be contaminated by a large amount of HNO_3 thought to be introduced from the NO_2 gas cylinder. This contamination was sufficient to deplete the primary reagent ions to a significant degree, which has been found in previous work to decrease the sensitivity of the instrument. The observed value is, therefore, a reasonable lower bound for the maximum sensitivity, while the theoretical value by definition provides an upper bound. These two values, 75 and 300 µncps ppt^{-1}, provide a well-constrained range of maximum sensitivity, S_{max}. This factor of 4 represents a major area of uncertainty in this work that can be greatly reduced in future experiments through improved N_2O_5 calibrations.

b. Particle-phase sensitivity

Particle-phase measurements by FIGAERO I^- CIMS are compared in this work to measurements by TD-AMS and SMPS both to validate the calibration approach developed here, and provide additional detail on the composition of pOC.

By accounting for pre-concentration of desorbed sample, and desorption volume, the sensitivity (discussed above) can be used to relate the analyte concentrations to the integral of measured signal over the desorption time, $\left(\frac{i_X}{i_P}\right)_{tot}$. The measurement of interest, the concentration of a compound *X* in the chamber, is by definition the ratio of total number of molecules sampled to volume sampled:

$$[X]_{cham} = \frac{N_{samp_{tot}}}{V_{collected}} \quad (4)$$

The total number of molecules sampled is by definition the sum across all timesteps, t, of the concentration in the sampled air, times the sampled volume in that timestep, which is in turn the sample flow (2 slpm) times the timestep:

$$N_{samp_{tot}} = \sum_t [X]_{samp_t} V_{samp_t} = \sum_t [X]_{samp_t} Q_{samp_t} \Delta t \quad (5)$$

The concentration of *X* in chamber air is therefore:

$$[X]_{cham} = \frac{\sum_t \left([X]_{samp_t} Q_{samp_t} \Delta t \right)}{V_{collected}} \quad (6)$$

which can be further substituted with equation (2) to remove dependence on the unknown concentration in the sampled air:

$$[X]_{cham} = \frac{\sum_t \left([M]_{samp_t} \frac{[X]_{IMR_t}}{f[M]_{IMR_t}} Q_{samp_t} \Delta t \right)}{V_{collected}} \quad (7)$$

The kinetic limit equation (1) can then be applied to determine the maximum sensitivity:

$$[X]_{cham} = \frac{\sum_t \left(\frac{[M]_{samp_t}}{f[M]_{IMR_t}} \frac{1}{k_{coll} t_{IMR}} \left(\frac{i_X}{i_P} \right)_t Q_{samp_t} \Delta t \right)}{V_{collected}} \quad (8)$$

Given that pressure changes in the IMR vary by less than 10%, most of the terms in the integral in equation (8) are approximately constant with time, including the total number of gas-phase molecules in both the IMR and the sample line, the collision rate, the residence time in the IMR, and the sample flow into the IMR. This equation can therefore be re-formulated as:

$$[X]_{cham} = \frac{\frac{[M]_{samp}}{f[M]_{IMR}} \frac{1}{k_{coll} t_{IMR}} Q_{samp}}{V_{collected}} \sum \left(\frac{i_X}{i_P} \right)_t \Delta t \quad (9)$$

The concentration of compound *X* in the chamber is therefore a function of several operational constants and the total normalized signal measured over the time of the sample desorption:

$$[X]_{cham} = \frac{\frac{[M]_{samp}}{f[M]_{IMR}} \frac{1}{k_{coll} t_{IMR}} Q_{samp}}{V_{collected}} \left(\frac{i_X}{i_P} \right)_{tot} \quad (10)$$

By combining equations (3) and (10), it can be shown that:

$$S_{kin,FIG} = \frac{\left(\frac{i_X}{i_P} \right)_{tot}}{ppt} = S_{kin} \frac{V_{collected}}{Q_{samp}} \quad (11)$$

As expected, particle-phase sensitivity with the FIGAERO, $S_{kin,FIG}$, is related to the kinetically limited gas-phase sensitivity through the volume collected, which increases sensitivity through concentration, and the desorption/sample flow, which decreases sensitivity through dilution. Note that S_{kin} and S_{FIG} differ in units by inverse time, because the signal term in the FIGAERO is the integral of signal over time. From equation (10), the maximum kinetically limited sensitivity of particle-phase measurements is calculated at 46000 counts per ppt per million reagent ions (µncps) as the upper bound maximum sensitivity. The discrepancy between theoretical and empirical sensitivity applies for particle-phase measurements as for the gas-phase above, so approximately 12000 counts per ppt per million reagent ions (µncps) is applied as the lower-bound maximum sensitivity.

2.2. *Strength of the ion-cluster bond*

Previous work by Iyer et al.[8] has demonstrated the binding energy of the analyte reagent ion cluster is log-linearly correlated to observed sensitivity. The binding energy can, in turn, be measured for all observed analytes through "de-clustering scans," in which the voltages of the front ion focusing components are ramped relative to the voltages of the rest of the instrument, the "skimmer" between the two quadrupoles marking the divide between front and back. This procedure, discussed in detail by Lopez-Hilfiker et al.[5] for an I- CIMS, produces a plot of the fraction of signal remaining at a given voltage difference, ΔV. A sigmoidal fit of the average de-clustering scan across the experiment yields two parameters: the voltage difference at which half of the signal is removed, dV_{50}, representing the de-clustering of half of the analyte-reagent ion clusters, and the relative amount of signal that would be present if the instrument could be operated at a lower voltage difference, S_0. dV_{50} is empirically correlated with binding energy and therefore sensitivity of the instrument to the analyte, while S_0 provides a multiplier of up to ~1.5[4,5,8] due to de-clustering of weakly bound clusters that can occur even at typical operating voltages. Analytes that stay clustered with the reagent ion even in the presence of relatively high ΔV are detected with maximum sensitivity (the threshold for this condition is determined below to be 6.3 V). De-clustering scanning is not effectively performed for FIGAERO particle-phase data because thermal desorption of each ion causes the concentration to vary substantially over the course of the scan, preventing an accurate measurement of dV_{50}. dV_{50} and S_0 are therefore assumed for particle-phase analytes to be equivalent to the same formulas observed in the gas phase. Particle-phase analytes that are not detected in the gas-phase are likely to be highly oxidized and are therefore assumed to be measured with maximum sensitivity.

The work of Iyer et al., Lee et al., and Lopez-Hilfiker et al.[4,5,8] has shown an empirical relationship between dV_{50} and sensitivity, S_X, with the cutoff for maximum sensitivity occurring at dV_{50} = 6.3V. Analytes with dV_{50} at or above this value are observed to de-cluster negligibly at typical operating voltages. Analytes with observed dV_{50} below this "inflection point" are observed to de-cluster to some degree at typical operating voltages, and are found to have a sufficiently weak binding energy to have a sensitivity lower than S_{max}. For analytes with a dV_{50} below this inflection point, sensitivity is observed to decrease by a factor of $10^{0.9}$ per volt due to the low binding energy, and already be partially de-clustered by a factor of S_0. Sensitivity of an analyte can therefore be estimated as:

$$S_X = \begin{cases} dV_{50,X} \geq 6.3 & : \quad S_{max} \\ dV_{50,X} < 6.3 & : \quad S_{max} S_{0,X} 10^{-0.9(6.3 - dV_{50,X})} \end{cases} \tag{12}$$

We find the inflection point, constrained by dV_{50} of N_2O_5 and malonic acid voltage scans (Supplementary Figure 1a), to be similar to the previously published value of 6.3V. The relative sensitivities of kinetically limited compounds, hydroxyacetone, and acetic acid were also measured and found to generally agree with those shown in Figure 6 of Iyer et al.[8] suggesting agreement of this instrument with the log-linear slope reported in that work. Equation (12) is therefore used as the fundamental relationship in this work, with uncertainty included as described below. Below a certain threshold for sensitivity, an analyte will not be observed by the instrument unless present in very high concentrations; this threshold is empirically found to correspond to dV_{50} = ~4V, with almost no analytes having a de-clustering voltage below this value other than a few major photooxidation products discussed in the main text. Supplementary Figure 1a also shows voltage scans of $C_3H_4O_4$ before and during an α-pinene photooxidation experiment; an ion of this formula is present in the background air, and it exhibits a

binding strength near that of malonic acid; however the ion produced through photooxidation has a substantially lower binding energy and so is an isomer of malonic acid, providing an example of voltage scans for weakly bound clusters.

The two parameters associated with the relationship between dV_{50} and S_X – the inflection point of 6.3 V and the log-linear slope of -0.9 S_X V^{-1} – are assumed to have a Gaussian distribution of uncertainty with a standard deviation of 0.125 S_X V^{-1}. Uncertainty in the inflection point is relatively small, as the measured value is reasonable well constrained and similar to reported values. However, uncertainty in the slope introduces significant uncertainty to the sensitivity of any given ion. Uncertainty increases as dV_{50}, decreases, reaching approximately an order of magnitude uncertainty in insensitively measured ions. This is consistent with the substantial scatter in dV_{50} of insensitively-detected analytes.[8] When dV_{50} of an analyte is near the threshold for measurement, uncertainty is so high that the instrument is functionally insensitive to the analyte and it cannot be reliably quantified unless explicitly calibrated with authentic standards (which may not be available). The calibration applied in this work was thus limited to a threshold of 2 orders of magnitude below maximum sensitivity. Analytes with lower dV_{50} are assigned a sensitivity of S_{max}/100 to avoid inclusion of species whose quantification is highly uncertain. The relationship between dV_{50} and S_X applied in this work is shown in Supplementary Figure 1b with the published relationship shown in black, and the range of uncertainty introduced shown in the red shaded region.

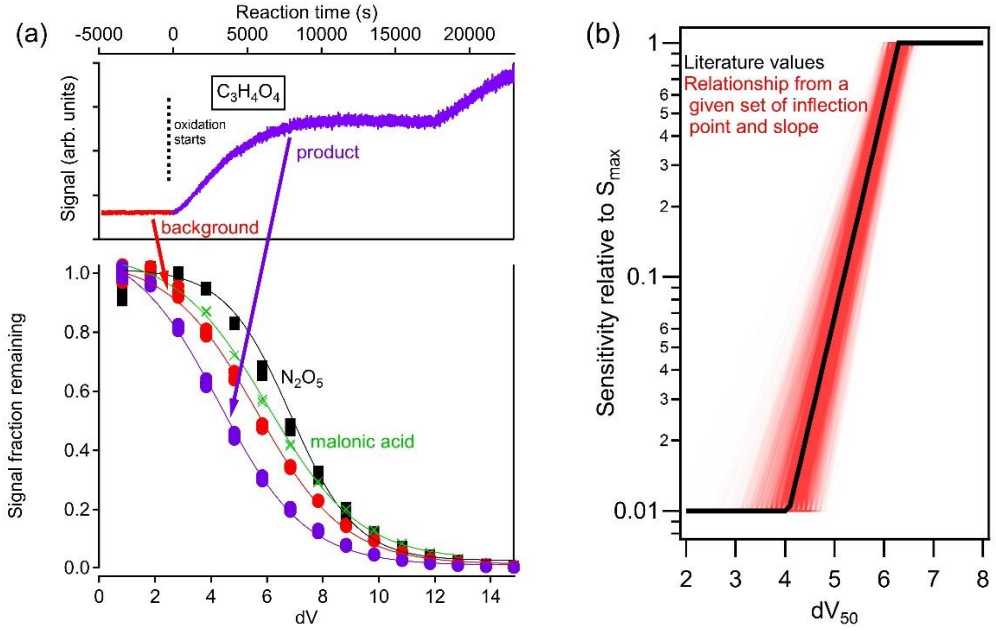

Supplementary Figure 1. (**a**) Voltage scans of maximum sensitivity compounds N_2O_5 (black squares) and malonic acid (green crosses), and ion $C_3H_4O_4$ measured in the photooxidation of α-pinene (time dependence shown in top panel). Voltage scan of background concentrations of this ion shown in red circles, and of the ion produced by photooxidation shown in purple circles. (**b**) Relationship between maximum sensitivity of the I- CIMS, S_{max}, and the voltage, dV_{50}, at which half of an analyte ion declusters. Relationship in the literature shown in black (including the cutoff of S_{max}/100 applied in this work). Red lines represent the range of values used in this work, with each red line representing one possible relationship within the distribution of uncertainty described in the main text.

The distribution of ions by dV_{50} observed in the experiments are shown in Supplementary Figure 2a-b compared to the average relationship between this parameter and S_X. Any insensitively-detected analytes (with dV_{50} below ~4 V) are potentially underestimated in this work. The choice of $S_{max}/100$ (equivalent dV_{50} = ~4V) as a threshold is arbitrary, but the results are generally insensitive to the assigned threshold because relatively little signal is in the vicinity of this threshold. The time-dependence and approximate calibration (based on values reported by Iyer and co-workers[8]) of the substantially underestimated ion in the case of photooxidation are similar to observed unmeasured mass (Supplementary Figure 9). Due to their extremely low sensitivity, these ions were obscured in the primary photooxidation experiment, and measured in a later repeat in which the FIGAERO inlet was removed from the I^- CIMS to yield cleaner background signals.

In addition to individual ions with low dV_{50} values, some ions may include multiple isomers, each of which may be differently sensitive due to differences in molecular structures or chemical functionality. The most sensitive ion will contribute disproportionately to the changes in signal observed in voltage scanning, resulting in a potential high bias in dV_{50} and (poorly quantified) underestimation of mass. Differences in isomeric sensitivity, and thus potential underestimation, are shown to be largest for less functionalized compounds.[4] This is expected because lightly functionalized compounds (with few functional groups per carbon atom) are more likely to have isomers for which the only available sites for reagent ion-analyte interactions are sterically hindered. As the number of functional groups increases relative to the carbon backbone, available sites for binding between the analyte and the reagent ion increase. This underestimation of isomers with few functional groups may contribute to unmeasured carbon, a possibility discussed below.

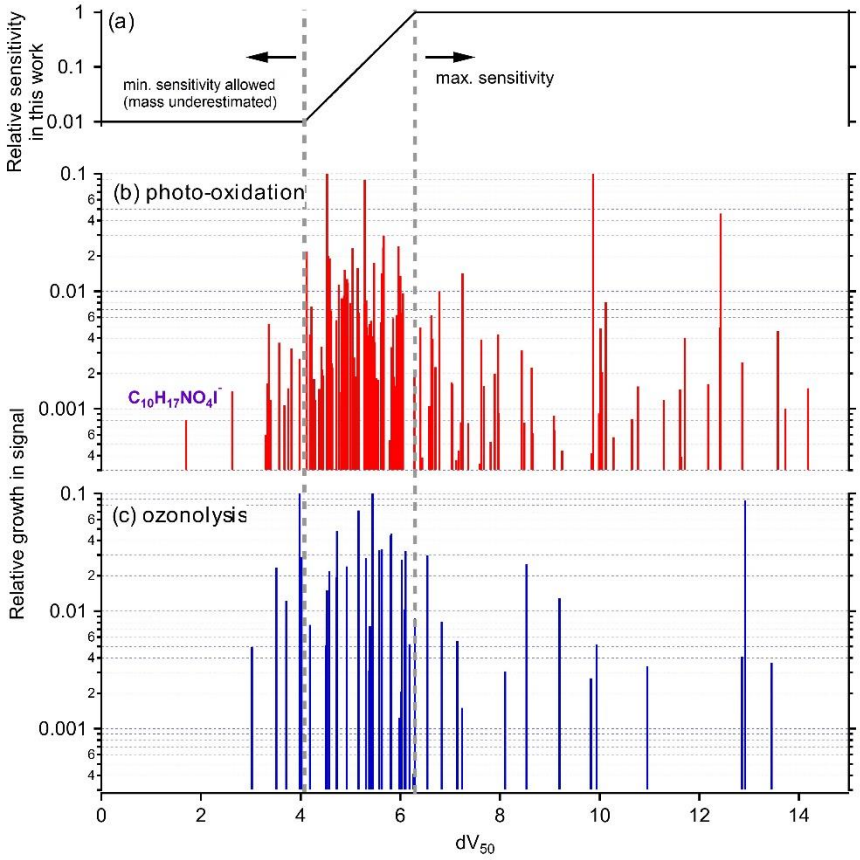

Supplementary Figure 2. (**a**) Relationship for I^- CIMS between sensitivity of an analyte relative to S_{max} and dV_{50} compared to observed distribution of signal in (**b**) photooxidation and (**c**) ozonolysis. Height of each ion is the growth in signal of that ion at its maximum point in the experiment as fraction of total growth in all ions. Signal at analyte-reagent cluster ion $C_{10}H_{17}NO_4I^-$ (discussed in Section S4) labeled in purple in panel (b).

2.3. Mass dependent transmission

Transmission an ion through any mass spectrometer is a function of the ion's molecular weight. This correction has been explored in detail for both time-of-flight CIMS and PTR-MS and can be empirically determined through introduction of known analytes across the mass spectral range of interest. In the case of CIMS measurements, however, this presents a challenge as few commercially available compounds are sufficiently volatile and sensitively measured by I^- CIMS to span the desired range of molecular weight. For this reason, perfluorinated acids are sometimes used for this purpose, but the strong adverse health effects of these compounds[28] limit their regular application and present a user risk. We consequently develop here an approach for the empirical correction of mass dependent transmission based on the dataset itself and not requiring introduction of additional compounds.

Samples collected by FIGAERO are sufficiently concentrated that desorption of the sample results in a moderate (10-15%) depletion in the primary reagent ions. If transmission of all ions was equal, the observed summed total ion count (TIC) would not be impacted by this depletion, but this is not the case.

The observed total ion signal decreases during desorption as analytes have higher molecular weight, and thus poorer transmission, than the reagent ions. The mixture of analytes necessarily spans the molecular weight range of interest, and the changing composition over the course of the experiments changes the average transmission. These features can be exploited to solve the average transmission function of the instrument.

A linear least squares approach can be solved for the matrix of data to determine coefficients (constrained to > 0) for each nominal mass that minimizes the deviation of the TIC from an arbitrary average value. The least linear squares solution is found to be noisy when coefficients at each mass are fully independent. There is no unique solution because multiple masses with similar variability (e.g. those that are noisy or have high backgrounds) are mathematically indistinguishable. However, earlier work by Heinritzi et al.[12] has demonstrated (Figure 5 of that reference) that the transmission function is expected to take the form of a modified Gaussian peak with a baseline that decreases with molecular weight. The fully empirical solution can therefore be compared to a constrained function approach, in which coefficients are optimized to describe a function of this form that minimizes the variability of the TIC. The constrained function approach is found to be in reasonably good agreement with the fully empirical solution, and correcting the observed ion signal by the optimized function produces a TIC with low variability (Supplementary Figure 3).

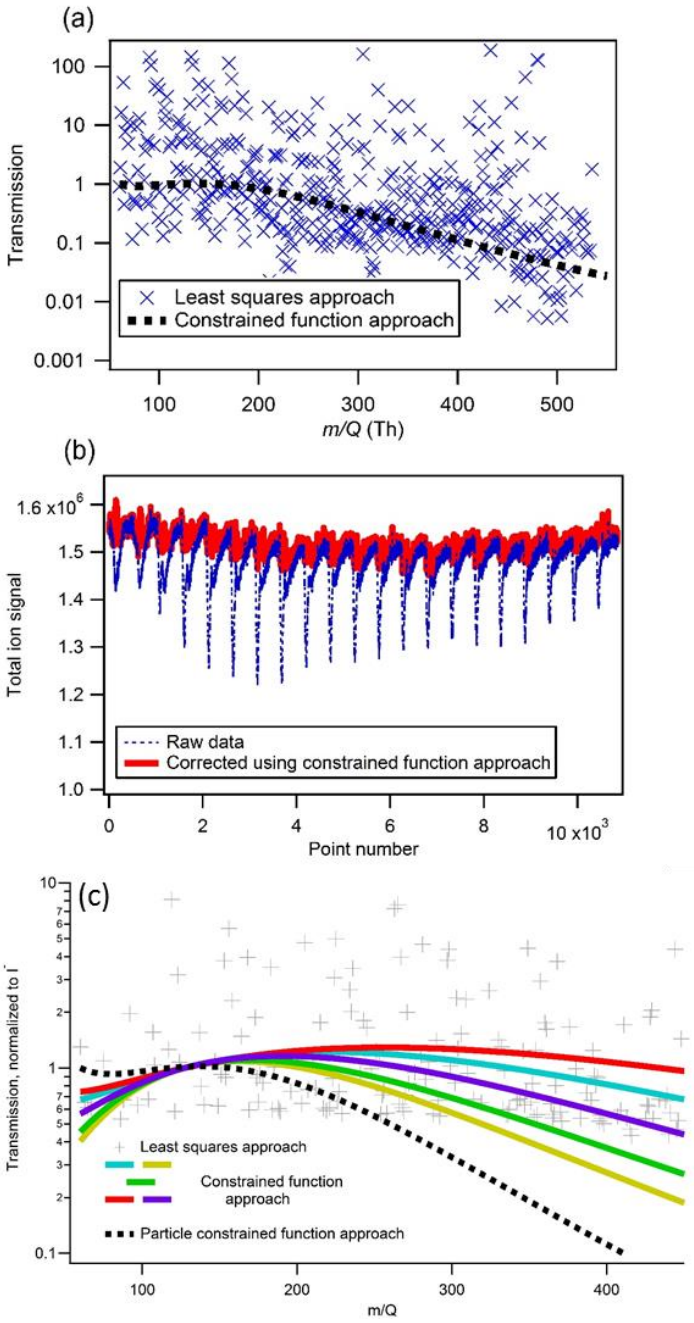

Supplementary Figure 3. Mass dependent transmission of the I^- CIMS data from oxidation by OH. (**a**) Observed transmission coefficients for FIGAERO data at each nominal mass shown using a linear least squares approach (blue crosses) and the constrained function approach assuming a modified Gaussian peak as the functional form (black dashed line). (**b**) Total ion signal measured by the I^- CIMS during FIGAERO desorption cycles using each approach. Raw observations shown in blue dashed line. Red line is after correction by the mass dependent transmission function shown as black dashed line in panel (a). (**c**) Five possible solutions bracketing the solution space of the constrained function approach for gas-phase data shown as colored lines. Empirical linear least squares approach shown as gray crosses. Function determined from FIGAERO data in panel (a) recreated as black dashed line.

The concentration in gas-phase samples does not deplete the primary reagent ions sufficiently to provide large variability in the TIC. Consequently, neither approach provides an ideal solution: the direct empirical approach is quite noisy, and the constrained function approach is not so well constrained, with several sets of optimized coefficients that produce relatively similar variability in the TIC. These coefficients therefore represent a range of possible mass-dependent transmission functions that are approximately bracketed by the cases shown in Supplementary Figure 3c. The black dashed line is the solution shown in Supplementary Figure 3a determined for the particle-phase measurements, which is observed to be similar to the gas-phase solutions, but decay somewhat more steeply than in gas-phase measurements. This may be due to increases in temperature caused by desorption, and differences in pressures in the IMR and other ion focusing components, which vary by 5% between operation modes. Since conducting these experiments and identifying this source of uncertainty, improvements to pressure regulation have been implemented that reduce variability to <1% between modes. We anticipate that this will enable the transmission function calculated from particle-phase measurements, which are well-constrained as shown in Supplementary Figure 3, to be applied to gas-phase measurements. Uncertainty introduced by poorly constrained mass dependent transmission will therefore be substantially reduced in the future.

2.4. Complete calibration

Four main contributors to uncertainty are identified here along with the values supported for each by the discussion above:

1. Maximum sensitivity, S_{max}: 75 or 300 (*equal chance of either*)
2. dV_{50} at which S_X goes to S_{max}: 6.3 V ± 0.125 (*s.d. of Gaussian distr.)*
3. Slope of relationship between dV_{50} and S_X: $10^{-0.9 \pm 0.125}\, S_X\, V^{-1}$ (*s.d. of Gaussian distr.*)
4. Mass dependent transmission: five functions in Supplementary Figure 3c (*equal chance of each*)

Though other parameters have associated error, such as uncertainty in S_0 and dV_{50} due to uncertainty in the sigmoidal fit of the de-clustering scan of each compound, such precision errors summed across all analytes are negligible in comparison to the four uncertainties listed above. Reported concentrations and uncertainty are calculated using a "Monte Carlo"-type approach, by performing 5000 calibrations, each using randomly selected parameters from the constraints listed above. The distribution of calibrated total mass concentrations are shown in Supplementary Figure 4a, with each individual calibration shown in translucent red. Overall uncertainty in total carbon measured by the I^- CIMS is 60%. Uncertainty in the calibration of any given ion is substantially higher, a factor of approximately 2.5 (geometric standard deviation), but these errors are uncorrelated, leading to lower relative uncertainty in total measured carbon.

Uncertainty in maximum sensitivity contributes the largest fraction of the error, as the term S_{max} affects sensitivity of all analytes. Total measured concentration is therefore linearly dependent on this parameter. In future studies, an empirical measurement of this parameter is expected to obtainable with only 10-20% uncertainty instead of a factor of 4. On the other hand, uncertainty in parameters 2 and 3 above, those from the de-clustering scans (illustrated in Supplementary Figure 1) are not expected to be substantially reduced in future experiments. Combined with the improvements implemented to reduce uncertainty in mass dependent transmission, future uncertainty for total mass measured by this instrument can be reduced from 60% to only 20%.

Most of these errors are uncorrelated, and thus mitigated by summing across all ions. However, the assumption that dV_{50} accurately represents the binding energy of all ions introduces a potential bias toward underestimation, since some "low-sensitivity" isomers may not be detected. This bias is expected to be correlated with number of functional groups, and is elucidated by Supplementary Figure 4b,c. An initial growth in unmeasured carbon is accompanied by growth in products with a range of initial products. However, the least oxygenated compounds measured by the I^- CIMS (with O:C < 0.33) are observed to correlate for the longest duration with total unmeasured carbon, and only lightly oxygenated compounds are observed to decrease in concentration with unmeasured carbon. Unmeasured carbon may therefore not only be due to "missing" ions not detected by these instruments, but also to "missing quantification" of isomers of ions with few functional groups or compounds with similar properties (i.e. lightly oxygenated functionalization products). Compounds with more available functional groups continue to grow in concentration during the depletion of unmeasured carbon and exhibit no correlation with unmeasured carbon, suggesting this effect is important mostly for the early-generation products.

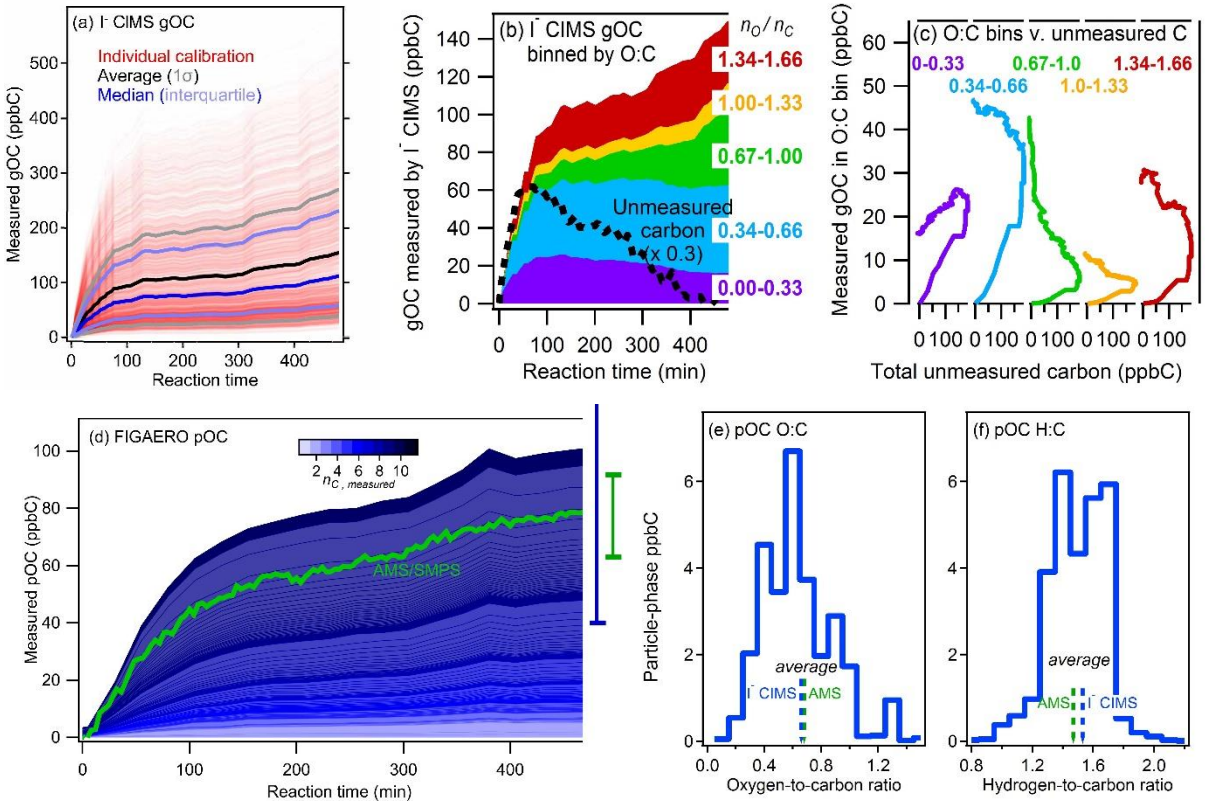

Supplementary Figure 4. Results from I^- CIMS calibration for the photooxidation experiment. (**a**) Gas-phase concentrations, where each translucent red line represents one of 5000 calibrations using a given set of parameters as described in the main text. Average (black, standard deviation in gray) and median (blue, interquartile range in light blue) of all calibrations shown. (**b**) Gas-phase concentrations binned by the oxygen-to-carbon ratio (O:C) of each ion (number of measured oxygens divided by number of measured carbons), with total unmeasured carbon show as a black dashed line, and (**c**) the correlation of each O:C bin to total unmeasured carbon. (**d**) Particle-phase concentrations measured by FIGAERO I- CIMS in blue, colored by the number of carbon atoms in each measured ion, and by SMPS/AMS in green. Uncertainty for both instruments shown as bars on the

right. Both instruments measured similar elemental compositions as shown for (**e**) oxygen-to-carbon ratio and (**f**) hydrogen-to-carbon ratio at a representative time (t = 270 min) with the average composition shown as dashed arrows (black: AMS, yellow: FIGAERO I^- CIMS).

To provide additional validation of this calibration approach, particle-phase composition measured by the FIGAERO I^- CIMS is shown in detail and compared to AMS measurements in Supplementary Figure 4d-f. Particle-phase carbon concentrations agree between these measurement techniques within instrument uncertainties, with a final wall-loss and dilution adjusted concentration of 78±16 ppbC measured by SMPS and AMS, and 100±60 ppbC measured by FIGAERO I^- CIMS. As shown in Supplementary Figure 4e,f, chemical composition of pOC as measured by these two instruments is also agree: the average oxygen-to-carbon ratio and hydrogen-to-carbon ratio measured by AMS (0.68 and 1.47 respectively) is near the center of the distributions, and similar to the averages, measured by FIGAERO I^- CIMS (0.66 and 1.53, respectively). These values are in approximate agreement with previous chamber experiments and moderately oxidized ambient OA.[29]

3. Calibration details: PTR-MS

Calibration of most ions measured by the PTR-MS was performed using a general reaction rate constant and mass-dependent transmission function measured by authentic standards and applied to all unidentified ions. α-pinene was calibrated explicitly by authentic standard. Compounds discussed and shown in this work as "identified ions" are treated explicitly. Acetic acid is reported as the sum of its molecular ion, $C_2H_4O_2$, and a known fragment ion, C_2H_2O. Acetone is reported as the concentration of C_3H_6O. Both gases are known products of this chemical system, so it is unlikely (though possible) that these ions represent other isomers with these formulas. In both cases, however fragmentation of larger compounds into these ions may increase their apparent concentrations, so reported concentrations of these compounds represent an upper bound. Similarly, HCHO is a common fragmentation product, so reported concentrations of formaldehyde are measured by TILDAS measurements and not reported for the PTR. Indeed, HCHO concentrations as measured by PTR are 2-3 times higher than those measured by TILDAS.

Uncertainty in the concentration of any given ion that has not been calibrated explicitly is 30%[30] due to variability in reaction rate constants.[31] Absolute error in each ion concentration is uncorrelated, so contribution of per-ion uncertainty to uncertainty in the total concentration of carbon measured by the PTR-MS is low. Instead, uncertainty is dominated by calibration uncertainty in the determination of the general reaction rate constant, uncertainty in instrument operating conditions (e.g. flow rates), and uncertainty in fragmentations of large ions discussed here.

3.1. Fragmentation

Concentrations of pinonaldehyde are reported following previous work.[32] Earlier approaches typically report concentration as the sum of ions identified as fragments of pinonaldehyde.[33] However, many ions in complex mixtures are non-specific to this compound, so we apply a new approach in which the concentration of $C_{10}H_{14}OH^+$ (m/Q = 151.112 Th, the most abundant pinonaldehyde fragment ion) is multiplied by a calibration factor to account for the contribution from all remaining ions. Pinonaldehyde was synthesized using the method described by McMurry et al.[34] with a purity of ~90% based on the

NMR spectrum, which matched with that reported by Chacon-Madrid et al.[35] The calibration factor was determined by the observed fragmentation of this authentic standard at the experimental operating conditions of the PTR-MS:

Supplementary Table 3. Observed fragmentation pattern for pinonaldehyde under the operating condition of E/N ratio of 124 Townsend.

Exact mass	*Ion formula*	*Relative response*
170.125	$^{13}CC_9H_{16}O_2H^+$	0.01
169.122	$C_{10}H_{16}O_2H^+$	0.12
152.115	$^{13}CC_9H_{14}OH^+$	0.12
151.112	$C_{10}H_{14}OH^+$	1.00
123.116	$C_9H_{14}H^+$	0.10
109.102	$C_8H_{12}H^+$	0.32
108.089	$^{13}CC_7H_{10}H^+$	0.07
107.086	$C_8H_{10}H^+$	0.67
99.079	$C_6H_{11}OH^+$	0.19
81.070	$C_6H_8H^+$	0.19
72.050	$^{13}CC_3H_6OH^+$	0.05
71.049	$C_4H_6OH^+$	0.78
Response relative to $C_{10}H_{16}O_2H^+$:		3.6
Carbon lost as neutral fragments: 24%		

In this experiment, all of the $C_{10}H_{14}OH^+$ is assumed to form from pinonaldehyde, and the corresponding fraction of the other fragments are removed from the concentrations of quantified unknown ions to avoid double-counting mass. Note that other first- and early-generation products may also fragment to $C_{10}H_{14}OH^+$, so this approach still carries some uncertainty and serves as an upper bound.

In the case of pinonaldehyde, 24% of carbon is lost as neutral fragments, which is observed consistently across terpenes and their first- and early-generation products. Three examples from the literature[36,37] are shown in Supplementary Table 4, with a range of 16-21% of carbon lost as neutral fragments. This trend extends to many smaller oxygenated compounds as well, with most aldehydes and alcohols down to 5 or 6 carbon atoms losing at least 10% of their carbon as neutral fragments.[38,39] These estimated losses of neutral carbon suggest underestimation in PTR-MS carbon concentrations and lead to the asymmetry in reported uncertainty.

Supplementary Table 4. Published fragmentation patterns in the PTR-MS of α-pinene and two monoterpene oxidation products, α-terpineol and nopinone. Spectra were obtained with E/N ratios similar to the PTR-MS operating conditions in this work. Top ion is molecular ion in all cases.

α-pinene

Mass	***Assumed formula***	***Relative response***
137	$C_{10}H_{16}H^+$	1.00
95	$C_7H_{10}H^+$	0.02
81	$C_6H_8H^+$	0.84
67	$C_5H_6H^+$	0.02
Carbon lost as neutral fragments: 19%		

nopinone

Mass	***Formula***	***Relative response***
139.112	$C_9H_{14}OH^+$	1.00
122.105	$^{13}CC_8H_{12}H^+$	0.06
121.102	$C_9H_{12}H^+$	0.58
96.058	$C_6H_7OH^+$	0.04
95.086	$C_7H_{10}H^+$	0.04
94.078	$C_7H_9H^+$	0.07
94.074	$^{13}CC_6H_9H^+$	0.03
93.070	$C_7H_8H^+$	0.20
83.050	$C_5H_6OH^+$	0.33
80.063	$C_6H_7H^+$	0.12
79.055	$C_6H_6H^+$	0.07
69.070	$C_5H_8H^+$	0.06
Carbon lost as neutral fragments: 21%		

α-terpineol

Mass	***Assumed formula***	***Relative response***
155	$C_{10}H_{18}OH^+$	0.03
137	$C_{10}H_{16}H^+$	1.00
95	$C_7H_{10}H^+$	0.04
81	$C_6H_8H^+$	0.79
69	$C_5H_8H^+$	0.01
Carbon lost as neutral fragments: 16%		

3.2. Deposition to inlet lines

Chamber air was sampled by the PTR-MS through a 1 m Teflon line, with a Teflon filter in-line to avoid instrument contamination from particles. This sample line provides ample surface for the adsorption of lower-volatility gases and subsequent re-volatilization that may impact the observed time-dependence of measurements. Through the experiments shown below, we find these inlet wall effects to contribute negligibly to concentrations measured by PTR-MS.

An approximately stable concentration of pinonaldehyde in a hexane solution was measured through various sampling line conditions (Supplementary Figure 5). When switching between pure air and solution, hexane equilibrates in less than a minute, so any lag in equilibration time for lower-volatility gases is due not to changes in instrument conditions or calibration system, but to inlet artifacts. Under conditions approximating the sampling conditions of this experiment (panel d), inlet equilibration times of 2 to 10 minutes are observed for pinonaldehyde, an intermediate volatility gas. This is a critical result that may substantially impact high time-resolution measurements of lower-volatility gases, but is negligible in the context of this work as the observed period of unmeasured mass is on the order of 1-2 hours.

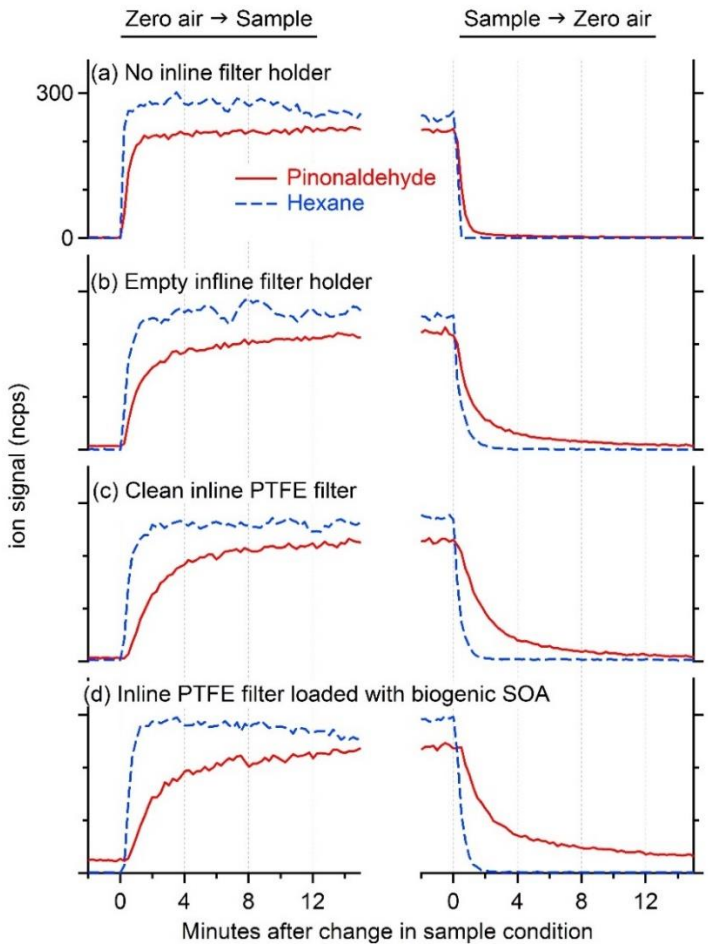

Supplementary Figure 5. Observed signal for a solution of pinonaldehyde (red solid line) in hexane (blue dashed line) under various sampling conditions, including (**a**) direct sampling through 1 m Teflon ¼"OD line, (**b**) the same line with an empty filter holder in line, (**c**) a clean PTFE filter in that holder, and (**d**) a PTFE filter in that holder that has been loaded by sampling α-pinene oxidation to approximate experiment conditions. Equilibration is shown (left) when switching from pure air to the solution and (right) when switching from solution to pure air.

4. Supporting results: photooxidation

4.1. Additional discussion

The evolving chemistry of photooxidation products is shown in Supplementary Figure 6; this is similar to Figure 3, but with a focus on individual phases/instruments: pOC measured by AMS (a-c), pOC measured by FIGAERO I^- CIMS (d-f), gOC only (g-i), and total gas- and particle-phase carbon including the α-pinene precursor (j-l) to show the evolution of the entire mixture (including reactants).

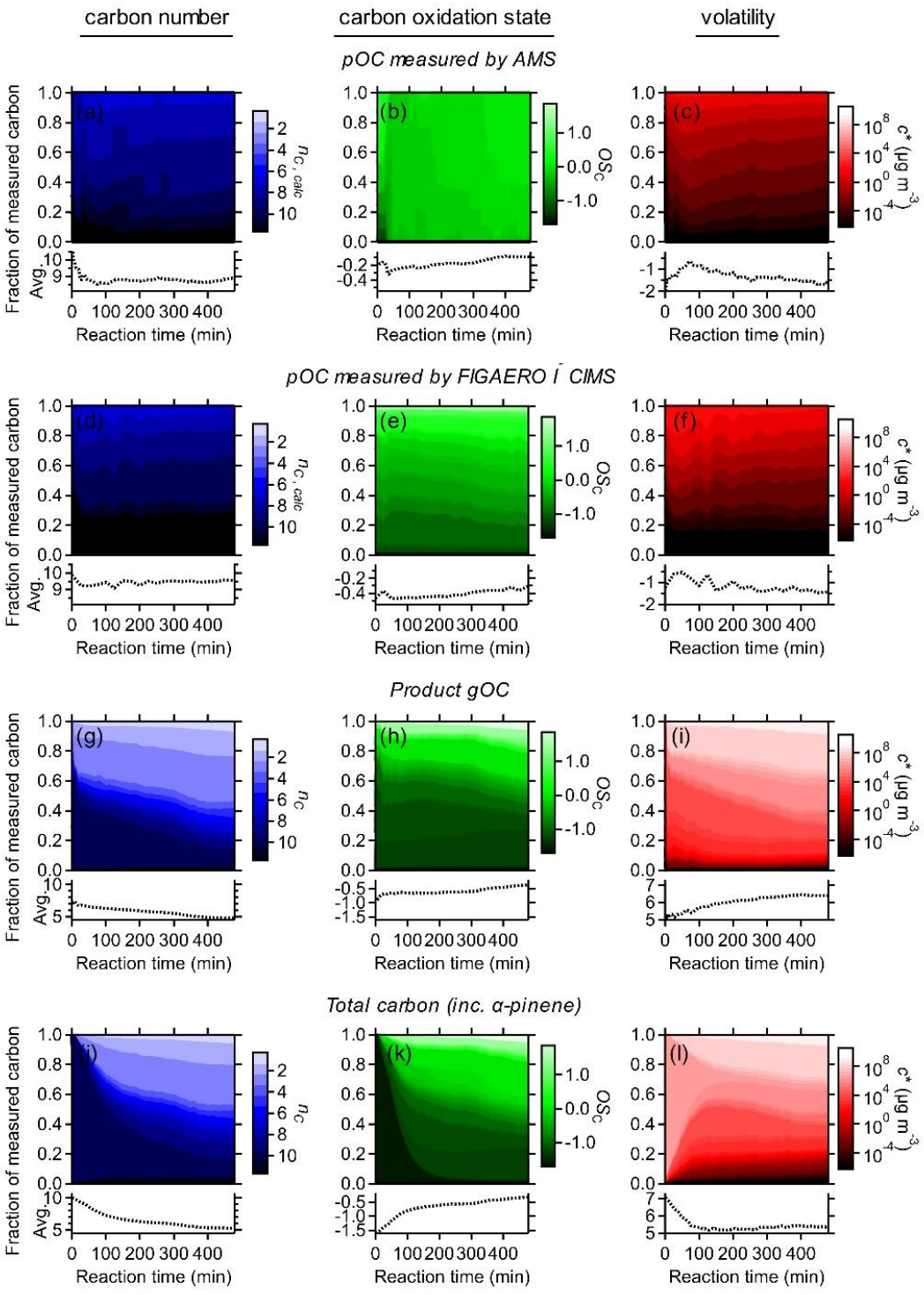

Supplementary Figure 6. Changing distributions of chemical properties of the photooxidation experiment as carbon-weighted normalized distributions. Properties shown are carbon number, oxidation state of carbon, and volatility, for (**a**-**c** respectively) pOC measured by TD-AMS, (**d**-**f** respectively) pOC measured by FIGAERO I^- CIMS , (**g**-**i** respectively) gas-phase product carbon, i.e. Figure 3 with pOC removed, and (**j**-**l** respectively) total gOC and pOC including precursor, i.e. Figure 3 with α-pinene included. The temporally evolving carbon-weighted averages of each property are shown as dashed lines in the bottom panels.

Of particular interest is the similarity between particle-phase composition as measured by both TD-AMS (panels a-c) and FIGAERO I^- CIMS (panels d-f). For the TD-AMS, volatility and oxidation state of carbon are directly measured, while carbon number is calculated ($n_{C,\,calc}$) based on *c** and elemental composition, following the relationships determined by Daumit et al.[40] Similarly, for the FIGAERO I^- CIMS data, $\overline{OS_C}$ is directly measured, and volatility can be directly measured based on the thermal desorption profile. However, carbon number can either be taken directly from formulas of measured ions ($n_{C,\,measured}$), or, as with the TD-AMS, estimated from the measured volatility and the elemental composition ($n_{C,\,calc}$). Previous work has shown that volatility measured directly through thermal desorption profiles more accurately describes the physicochemical properties of organic aerosol than the volatility inferred from the molecular formulas of observed ions. This is due to decomposition that occurs upon thermal desorption in the FIGAERO I^- CIMS, fragmenting accretion products into smaller constituent components and biasing measured ions toward smaller, more volatile species.[41,42] In Supplementary Figure 6, carbon number for FIGAERO I^- CIMS is therefore estimated from volatility and elemental composition ($n_{C,\,calc}$), as it is not only in agreement with the calculated TD-AMS values, but is also likely a more accurate representation of pOC composition. Note that the carbon number of each measured ion ($n_{C,\,measured}$) shown in Supplementary Figure 4d is generally substantially lower than the distribution of $n_{C,\,calc}$ due to decomposition of larger compounds. $\overline{OS_C}$ distributions are different between instruments because AMS measures an average $\overline{OS_C}$ for each volatility bin, while FIGAERO I^- CIMS provides a more complete distribution, since decomposition of accretion products into constituent compounds is not expected to substantially change $\overline{OS_C}$. Note that average AMS $\overline{OS_C}$ is near the center of the FIGAERO I^- CIMS distribution (see also Supplementary Figure 4). Given that these two instruments are in close agreement on particle composition, TD-AMS data is used in the main text as it has higher time resolution and lower uncertainty than the FIGAERO I^- CIMS.

The dynamics of the average trends in properties of product carbon shown in Figure 3 are shown as constituent gas- and particle-phase components in Supplementary Figure 6. Gas-phase product carbon initially has high n_C, low $\overline{OS_C}$, and intermediate volatility, likely comprised of functionalized products as discussed in the main text. Oxidation tends to monotonically decrease average n_C, increase oxidation, and increase volatility, suggesting products primarily fragment. Products of any later functionalization reactions are not clearly observed in the gas-phase, as they would likely to be lower in volatility and so would mostly condense and contribute to pOC. In photooxidation, pOC is first formed from these functionalized products, with an initial composition of high n_C, moderate $\overline{OS_C}$, and relatively low volatility. As this initial mass of pOC forms and grows, more volatile compounds partition into the particle phase, leading to an increase in volatility and decrease in carbon number. As the particles continue to oxidize, they incorporate oxygen with no substantial change in n_C, leading to a decrease in volatility and no apparent evidence for loss or fragmentation of pOC. The overall trends in average properties, and relatively dynamic behavior of the average *c**, shown in Figure 3 are the combination of these dominant chemical pathways: gas-phase fragmentation, and particle-phase formation, growth, and aging.

Total concentration of species measured by the NO_3^- CIMS (Supplementary Figure 7) accounts for less than 2 ppbC, less than 0.5% of total carbon and less than 2.5% of product carbon at all reaction times. This instrument measures extremely low-volatility, highly oxidized gases, so then fraction of product carbon peaks at the start of the experiment, rapidly decaying due to condensation onto suspended particles.

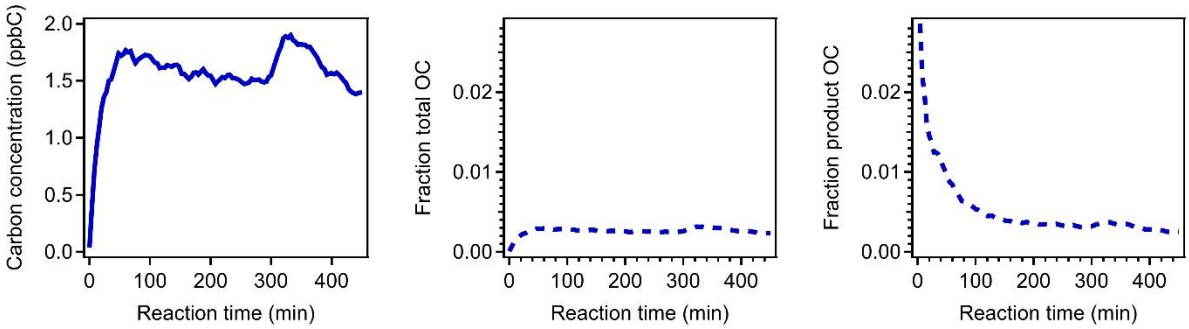

Supplementary Figure 7. Total concentration of species measured by NO_3^- CIMS as (a) carbon concentration, (b) fraction of total OC, and (c) fraction of measured product OC (α-pinene excluded).

4.2. Videos

Videos of the time-evolving composition of the photooxidation experiment as a function of oxidation state vs. both carbon number and saturation concentration (after Fig. 2) are available online as Supplementary Videos 1 ($\overline{\mathrm{OS_C}}$ vs. *c**) and 2 ($\overline{\mathrm{OS_C}}$ vs. n_C):

Supplementary Video 1. Chemical characterization of carbon measured in the photooxidation of α-pinene in terms of two parameters commonly used for simplified representations of atmospheric organic carbon: oxidation state of carbon ($\overline{\mathrm{OS_C}}$) and saturation concentration (*c**). By achieving carbon closure, these measurements yield a detailed understanding of the distribution of carbon in this chemical space and the evolution of chemical properties of carbon. Circle area is proportional to carbon concentration, colored by instrument. Dark gray: α–pinene; light gray: TILDAS; green: AMS/SMPS; purple: PTR-MS; orange: I^- CIMS; blue NO_3^- CIMS. pOC shown at average $\overline{\mathrm{OS_C}}$ of each volatility bin measured by TD-AMS. Average properties are shown as lines for pOC (green) and gOC (red solid: product, red dashed: total inc. α-pinene).

Supplementary Video 2. Chemical characterization of carbon measured in the photooxidation of α-pinene in terms of two parameters commonly used for simplified representations of atmospheric organic carbon: oxidation state of carbon ($\overline{\mathrm{OS_C}}$) and number of carbon atoms (n_C). By achieving carbon closure, these measurements yield a detailed understanding of the distribution of carbon in this chemical space and the evolution of chemical properties of carbon. Circle area is proportional to carbon concentration, colored by instrument. Dark gray: α–pinene; light gray: TILDAS; green: AMS/SMPS; purple: PTR-MS; orange: I^- CIMS; blue NO_3^- CIMS. pOC is shown at average $\overline{\mathrm{OS_C}}$ and n_C of each volatility bin measured by TD-AMS. Average properties are shown as lines for pOC (green) and gOC (red solid: product, red dashed: total inc. α-pinene).

4.3. Gas-particle-wall partitioning

A partitioning model was used to estimate fraction of carbon on the walls of the chamber following the approach of La et al.[43]. The timescale for gas-wall partitioning for all compounds was assumed to be 15 minutes based on the mixing time of the chamber and the empirical work of Krechmer et al.[44] in a similarly sized chamber. Absorption to the chamber wall depends on the "equivalent mass concentration of the wall," which was parameterized as described in Table 1 of that same reference. The timescale for gas-particle partitioning was assumed to be 10 seconds based on the condensation sink[45] calculated from the suspended surface area concentration. The fraction of a given volatility bin expected to be on the wall was modeled as a function of equilibration time, assuming reversible gas-wall and gas-particle partitioning.

The model is run to include or not include continuous OH reaction. Further gas-phase reaction by OH in this model (with assumed $k_{OH} = 2\times10^{11}$ cm^3 molec^{-1} s^{-1}) produces species that do not partition further, both for simplicity and based on the observations that later products are primarily high- and low-volatility compounds that are not quickly lost to walls. Depletion of a gas-phase compound through reaction with OH drives re-volatilization of condensed-phase components, which somewhat decreases the fraction of carbon deposited to the wall, particularly at longer equilibration times (Supplementary Figure 8a-b). The region of volatility most impacted by deposition to walls (IVOCs) is the region shown to be comprised of reactive first-generation products.

Carbon in each volatility bin at a given reaction time is expected to have a component on the wall under the assumption that equilibration of that carbon and further reaction with OH has been occurring since the start of reaction. That is, carbon in bin *i* at time *t* has a wall fraction assuming it has partitioned and reacted with OH for *t* minutes. Measured carbon in bin *i* therefore constrains carbon on the wall. For instance, if 80% of carbon in a bin is expected to be on the walls after 1 hour, then any suspended carbon measured in that bin at 1 hour must be complemented by four times more carbon on the wall (e.g. Supplementary Figure 8c-d). The timescale for gas-wall partitioning is fast compared to reaction times and loss of pOC to walls, so any changes to volatility distributions during equilibration are likely minor. Due to the relatively fast partitioning times relative to the length of the experiment, partitioning fractions equilibrate quickly, then change only slowly with time (see Supplementary Figure 8, panel a vs. panel b). Observed carbon closure at the end of experiments supports this model of vapor deposition as reversible, not irreversible.

From the observed volatility distribution, a majority of carbon has a volatility that are expected to be predominated gas or particle phase. Only a relatively small fraction is in the range of the volatility distribution that is most susceptible to deposition to walls ($c^* = 10^1$-10^5). Consequently, relatively little carbon is expected to be on walls at any moment. This fraction decreases with continued oxidation, with only ~10% of total carbon modeled to be on the wall by the end of the experiment. The time dependence of modeled reversible deposition to walls is similar but not identical to that of unmeasured carbon, suggesting this process may contribute in part to the gap in carbon closure at the beginning of the experiment.

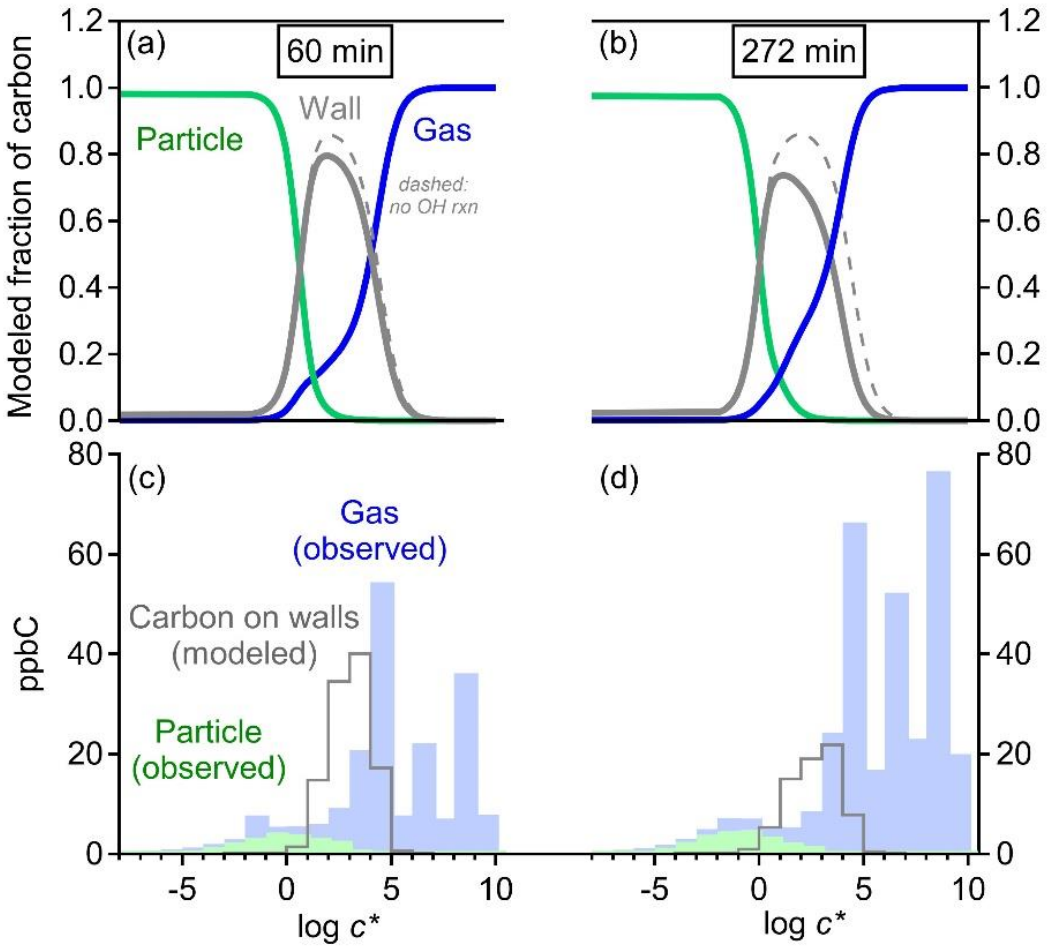

Supplementary Figure 8. Loss of carbon to the walls of the reaction chamber modeled for the photooxidation experiment as equilibrium partitioning and reaction with OH of measured carbon volatility distributions. Fraction of carbon of a given volatility in each phase after (**a**) the peak of unmeasured carbon at 60 minutes and (**b**) immediately prior to additional oxidation at 270 minutes are shown. Measured volatility distributions at these times are shown in (**c**) and (**d**), respectively. Particle-phase carbon in green, carbon on walls in gray, gas-phase carbon in blue including product of reaction with OH. Dashed gray line in top panels is modeled fraction on wall in the absence of continued reaction with OH.

4.4. Unmeasured carbon

The observed gap in measured carbon approximately matches both the measured concentrations of ions to which all instruments are poorly sensitive, and the modeled time evolution of carbon on walls (Supplementary Figure 9). In both cases (discussed below), unmeasured carbon is expected to be lightly functionalized IVOCs.

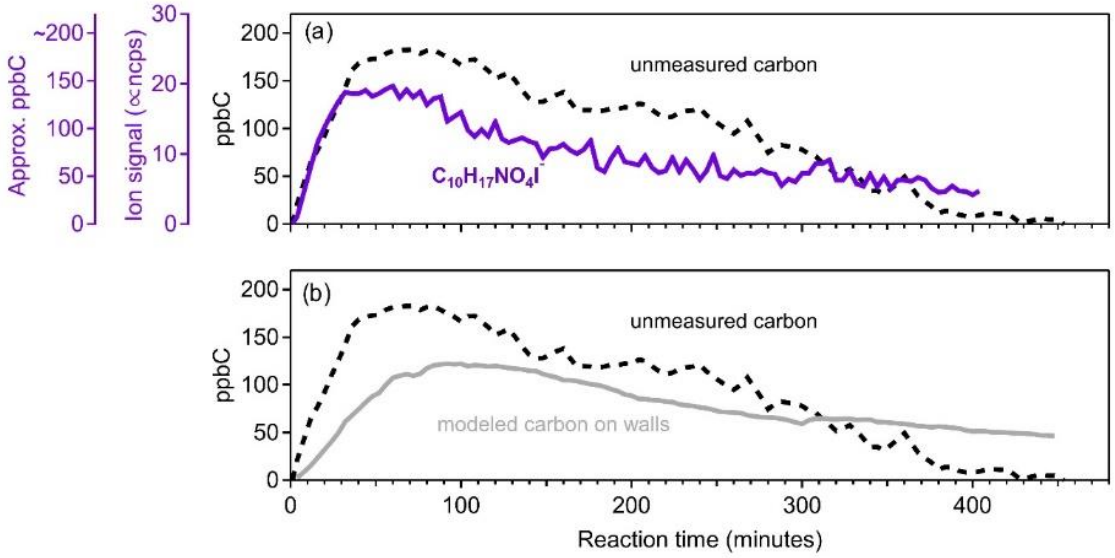

Supplementary Figure 9. Time evolution of unmeasured carbon compared to (**a**) $C_{10}H_{17}NO_4$ detected by the I^- CIMS, including approximate calibration, and (**b**) modeled carbon on walls at each time, based on model described above.

Low-sensitivity species. Sensitivity of the I^- CIMS generally increases with number of functional groups, so lightly oxidized compounds are poorly quantified regardless of volatility. Fragmentation to smaller ions upon analysis by PTR-MS increases with carbon number, in particular for oxygenated compounds. This issue, combined with the potential loss of lower-volatility species to PTR-MS inlet walls, makes lightly functionalized IVOCs beyond the region of viable measurement by this instrument. Consequently, I^- CIMS measures more-oxidized and/or lower-volatility species, while PTR-MS measures higher-volatility, and neither instrument accurately quantifies lightly functionalized IVOCs. $C_{10}H_{17}NO_4$ (likely α-pinene hydroxynitrate) is a lightly oxidized functionalization product at the edge of the viable range for measurement by I^- CIMS; it is detected but with very low sensitivity, on the order of 4000 times (published[8]) to 7000 times (calculated from ion-cluster strength) less sensitive than maximum sensitivity. Approximate calibration of this ion yields concentrations similar in magnitude (and time evolution) to unmeasured carbon in the photooxidation experiment (Supplementary Figure 9a). It is likely that other minor first-generation products similar to this species are produced but poorly quantified by this instrument suite.

Deposition to walls. The other possible explanation for the transient observation of unmeasured carbon is the reversible deposition and later re-volatilization of carbon to reactor walls (primarily comprised of IVOCs per Supplementary Figure 8). Compared to unmeasured carbon, modeled carbon on walls throughout the experiment (as described above) is lower in concentration, though within a factor of two (Supplementary Figure 9b). However, modeled carbon on walls persists longer into the experiment and is never fully re-suspended; this is in contrast to the carbon closure observed in measurements, suggesting that the model may overestimate wall loss somewhat. Carbon reversibly deposited to chamber walls therefore may contribute to, but is unlikely to fully account for, the unmeasured carbon. Partitioning to walls of inlets may also occur, but the observed (see Supplementary Fig. 5) and published[46] timescales for this process are shorter than the observed gap in measured carbon.

5. Supporting results: ozonolysis

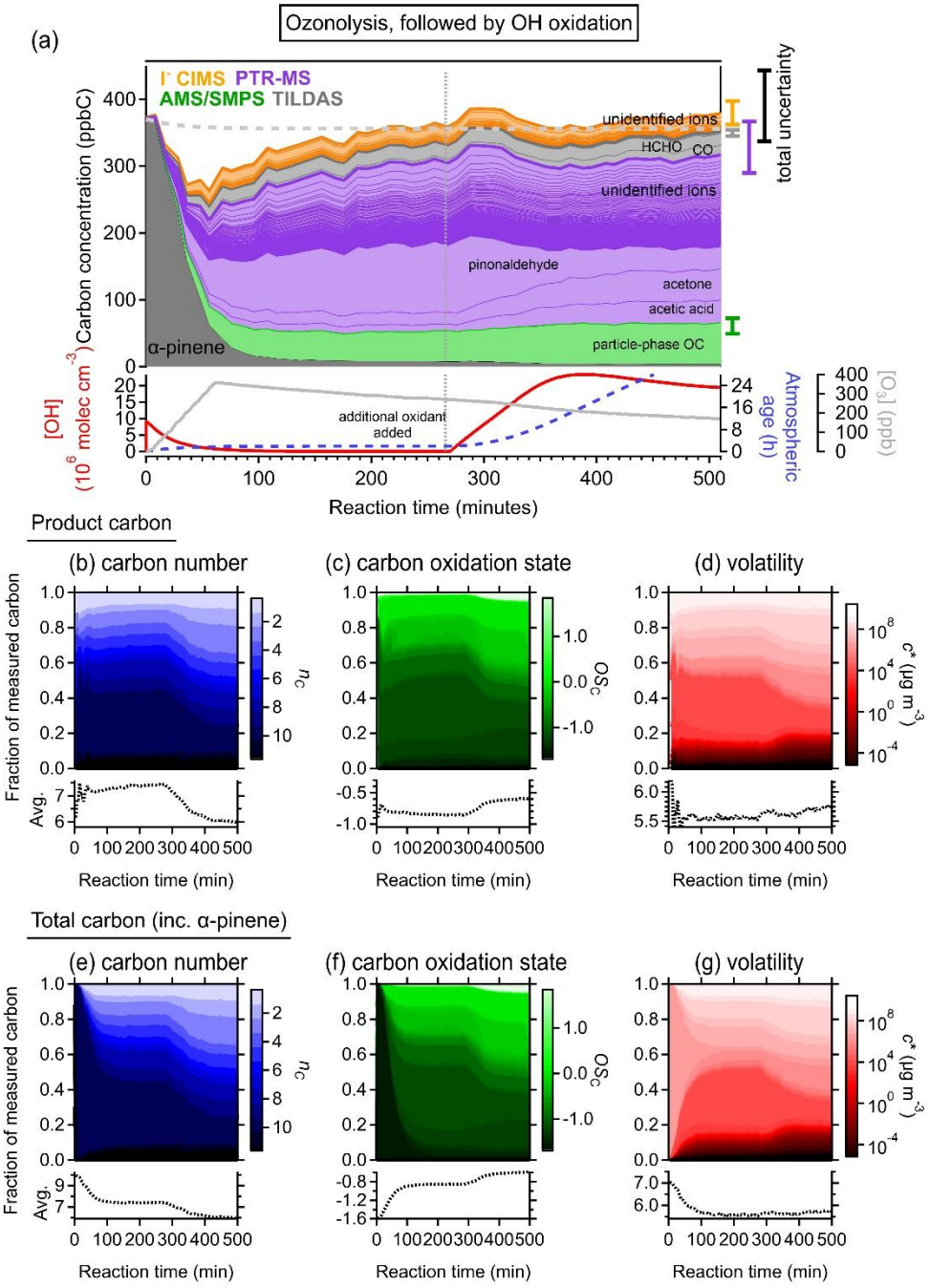

Supplementary Figure 10. Product mixture of ozonolysis followed by multi-generational oxidation by OH. Color scales and descriptions analogous to Figures 1, 3, and S6, reproduced in brief here. (**a**) Stacked concentrations of all measured compounds, colored by with which they are measured. Total carbon in the system (accounting for dilution) shown as gray solid line near initial concentration. Bottom panel shows oxidant levels and approximate atmospheric age assuming [OH] = 2×10^6 molec cm^{-3}. Distribution of chemical properties of measured product carbon shown for (**b**) carbon number, (**c**) oxidation state, and (**d**) volatility, and (**e-g**) total carbon including α-pinene and all products for the same respective properties. Average of each property shown as dashed line in bottom panels.

Time-dependent carbon closure and chemical properties of product mixture during ozonolysis is shown in Supplementary Figure 10, analogous to photooxidation figures (Figure 1, Figure 3, and Supplementary Figure 6). Initial reaction is reaction with ozone, followed by multi-generational oxidation by OH. The trends discussed in the main text are also observed in this experiment. Initial oxidation occurs through formation of compounds with large carbon numbers and intermediate volatility. Upon further oxidation, these compounds fragment into smaller, higher-volatility gas-phase compounds. Concurrent formation of additional low-volatility particle-phase mass yields the same tendency to diverge toward two pools of long-lived carbon. A small amount of unmeasured carbon forms in the initial oxidation, then decays away. The timescale for this process in the ozonolysis experiment is, in contrast with the photooxidation experiment, comparable to that of reversible deposition of intermediate-volatility gases to inlet walls;[46] inlet lags due to wall interactions thus may contribute in part to early gaps in carbon closure. Decay of unmeasured carbon may also be the result of formation of OH from initial ozonolysis, continuing oxidation of difficult-to-measure early generation products generated in the α-pinene plus ozone reaction.

6. References

1. Hunter, J. F., Carrasquillo, A. J., Daumit, K. E. & Kroll, J. H. Secondary organic aerosol formation from acyclic, monocyclic, and polycyclic alkanes. *Environ. Sci. Technol.* **48,** 10227–10234 (2014).

2. Wolfe, G. M., Marvin, M. R., Roberts, S. J., Travis, K. R. & Liao, J. The framework for 0-D atmospheric modeling (F0AM) v3.1. *Geosci. Model Dev.* **9,** 3309–3319 (2016).

3. Stark, H. *et al.* Methods to extract molecular and bulk chemical information from series of complex mass spectra with limited mass resolution. *Int. J. Mass Spectrom.* **389,** 26–38 (2015).

4. Lee, B. H. *et al.* An Iodide-Adduct High-Resolution Time-of-Flight Chemical- Ionization Mass Spectrometer: Application to Atmospheric Inorganic and Organic Compounds. *Environ. Sci. Technol.* **48,** 6309–6317 (2014).

5. Lopez-Hilfiker, F. D. *et al.* Constraining the sensitivity of iodide adduct chemical ionization mass spectrometry to multifunctional organic molecules using the collision limit and thermodynamic stability of iodide ion adducts. *Atmos. Meas. Tech.* **9,** 1505–1512 (2016).

6. Lopez-Hilfiker, F. D. *et al.* A novel method for online analysis of gas and particle composition: Description and evaluation of a filter inlet for gases and AEROsols (FIGAERO). *Atmos. Meas. Tech.* **7,** 983–1001 (2014).

7. Yatavelli, R. L. N. *et al.* A Chemical Ionization High-Resolution Time-of-Flight Mass Spectrometer Coupled to a Micro Orifice Volatilization Impactor (MOVI-HRToF-CIMS) for Analysis of Gas and Particle-Phase Organic Species. *Aerosol Sci. Technol.* **46,** 1313–1327 (2012).

8. Iyer, S., Lopez-Hilfiker, F. D., Lee, B. H., Thornton, J. A. & Kurtén, T. Modeling the Detection of Organic and Inorganic Compounds Using Iodide-Based Chemical Ionization. *J. Phys. Chem. A* **120,** 576–587 (2016).

9. Graus, M., Müller, M. & Hansel, A. High resolution PTR-TOF: Quantification and Formula Confirmation of VOC in Real Time. *J. Am. Soc. Mass Spectrom.* **21,** 1037–1044 (2010).

10. Jordan, A. *et al.* A high resolution and high sensitivity proton-transfer-reaction time-of-flight mass spectrometer (PTR-TOF-MS). *Int. J. Mass Spectrom.* **286,** 122–128 (2009).

11. Holzinger, R. PTRwid: A new widget tool for processing PTR-TOF-MS data. *Atmos. Meas. Tech.* **8,** 3903–3922 (2015).

12. Heinritzi, M. *et al.* Characterization of the mass-dependent transmission efficiency of a CIMS. *Atmos. Meas. Tech.* **9,** 1449–1460 (2016).

13. Park, J.-H. *et al.* Active Atmosphere-Ecosystem Exchange of the Vast Majority of Detected Volatile Organic Compounds. *Science* **341,** 643–648 (2013).

14. Taipale, R. *et al.* Technical Note: Quantitative long-term measurements of VOC concentrations by PTR-MS – measurement, calibration, and volume mixing ratio calculation methods. *Atmos. Chem. Phys. Discuss.* **8,** 9435–9475 (2008).

15. Jokinen, T. *et al.* Atmospheric sulphuric acid and neutral cluster measurements using CI-APi-TOF. *Atmos. Chem. Phys.* **12,** 4117–4125 (2012).

16. Krechmer, J. E. *et al.* Formation of Low Volatility Organic Compounds and Secondary Organic Aerosol from Isoprene Hydroxyhydroperoxide Low-NO Oxidation. *Environ. Sci. Technol.* **49,** 10330–10339 (2015).

17. Eisele, F. L. & Tanner, D. J. Measurement of the gas phase concentration of H_2SO_4 and methane sulfonic acid and estimates of H_2SO_4 production and loss in the atmosphere. *J. Geophys. Res.* **98,** 9001–9010 (1993).

18. Ehn, M. *et al.* A large source of low-volatility secondary organic aerosol. *Nature* **506,** 476–479 (2014).

19. Jokinen, T. *et al.* Production of extremely low volatile organic compounds from biogenic emissions : Measured yields and atmospheric implications. *Proc. Natl. Acad. Sci.* **112,** 7123–7128 (2015).

20. Decarlo, P. F. *et al.* Field-Deployable, High-Resolution, Time-of-Flight Aerosol Mass Spectrometer. *Anal. Chem.* **78,** 8281–8289 (2006).

21. Faulhaber, A. E. *et al.* Characterization of a thermodenuder-particle beam mass spectrometer system for the study of organic aerosol volatility and composition. *Atmos. Meas. Tech.* **2,** 15–31 (2009).

22. Sueper, D. ToF-AMS Analysis Software. (2010).

23. Canagaratna, M. R. *et al.* Elemental ratio measurements of organic compounds using aerosol mass spectrometry: Characterization, improved calibration, and implications. *Atmos. Chem. Phys.* **15,** 253–272 (2015).

24. Kuwata, M., Zorn, S. R. & Martin, S. T. Using elemental ratios to predict the density of organic material composed of carbon, hydrogen, and oxygen. *Environ. Sci. Technol.* **46,** 787–794 (2012).

25. McManus, J. B. *et al.* Pulsed quantum cascade laser instrument with compact design for rapid, high sensitivity measurements of trace gases in air. *Appl. Phys. B Lasers Opt.* **92,** 387–392 (2008).

26. Rothman, L. S. *et al.* The HITRAN2012 molecular spectroscopic database. *J. Quant. Spectrosc.*

809 *Radiat. Transf.* **130,** 4–50 (2013).

810 27. Huey, L. G., Hanson, D. R. & Howard, C. J. Reactions of SF6- and I- with Atmospheric Trace Gases.
811 *J. Phys. Chem.* **99,** 5001–5008 (1995).

812 28. United States Environmental Protection Agency. Drinking Water Health Advisory for
813 Perfluorooctanoic Acid (PFOA). 1–103 (2016).

814 29. Kroll, J. H. *et al.* Carbon oxidation state as a metric for describing the chemistry of atmospheric
815 organic aerosol. *Nat. Chem.* **3,** 133–139 (2011).

816 30. Park, J.-H. *et al.* Eddy covariance emission and deposition flux measurements using proton
817 transfer reaction – time of flight – mass spectrometry (PTR-TOF-MS): comparison with PTR-MS
818 measured vertical gradients and fluxes. *Atmos. Chem. Phys.* **13,** 1439–1456 (2013).

819 31. Zhao, J. & Zhang, R. Proton transfer reaction rate constants between hydronium ion (H3O+) and
820 volatile organic compounds. *Atmos. Environ.* **38,** 2177–2185 (2004).

821 32. Lee, A. *et al.* Gas-phase products and secondary aerosol yields from the photooxidation of 16
822 different terpenes. *J. Geophys. Res. Atmos.* **111,** D17305 (2006).

823 33. Wisthaler, A., Jensen, N. R., Winterhalter, R., Lindinger, W. & Hjorth, J. Measurements of acetone
824 and other gas phase product yields from the OH-initiated oxidation of terpenes by proton-
825 transfer-reaction mass spectrometry (PTR-MS). *Atmos. Environ.* **35,** 6181–6191 (2001).

826 34. McMurry, J. E. & Bosch, G. K. Synthesis of macrocyclic terpenoid hydrocarbons by intramolecular
827 carbonyl coupling: bicyclogermacrene, lepidozene, and casbene. *J. Org. Chem.* **52,** 4885–4893
828 (1987).

829 35. Chacon-Madrid, H. J., Murphy, B. N., Pandis, S. N. & Donahue, N. M. Simulations of smog-
830 chamber experiments using the two-dimensional volatility basis set: Linear oxygenated
831 precursors. *Environ. Sci. Technol.* **46,** 11179–11186 (2012).

832 36. Tani, A. Fragmentation and reaction rate constants of terpenoids determined by proton transfer
833 reaction-mass spectrometry. *Environ. Control Biol.* **51,** 23–29 (2013).

834 37. Steitz, B. Experimental determination of the partitioning coefficient of nopinone as a marker
835 substance in organic aerosol. (Bergischen Universitat Wuppertal, 2012).

836 38. Klein, F. *et al.* Characterization of Gas-Phase Organics Using Proton Transfer Reaction Time-of-
837 Flight Mass Spectrometry: Cooking Emissions. *Environ. Sci. Technol.* **50,** 1243–1250 (2016).

838 39. Buhr, K., Van Ruth, S. & Delahunty, C. Analysis of volatile flavour compounds by Proton Transfer
839 Reaction-Mass Spectrometry: Fragmentation patterns and discrimination between isobaric and
840 isomeric compounds. *Int. J. Mass Spectrom.* **221,** 1–7 (2002).

841 40. Daumit, K. E., Kessler, S. H. & Kroll, J. H. Average chemical properties and potential formation
842 pathways of highly oxidized organic aerosol. *Faraday Discuss.* **165,** 181–202 (2013).

843 41. Stark, H. *et al.* Impact of Thermal Decomposition on Thermal Desorption Instruments : Advantage
844 of Thermogram Analysis for Quantifying Volatility Distributions of Organic Species. *Environ. Sci.*
845 *Technol.* **51,** 8491–8500 (2017).

846 42. Lopez-Hilfiker, F. D. *et al.* Molecular Composition and Volatility of Organic Aerosol in the

Southeastern U.S.: Implications for IEPOX Derived SOA. *Environ. Sci. Technol.* **50,** 2200–2209 (2016).

43. La, Y. S. *et al.* Impact of chamber wall loss of gaseous organic compounds on secondary organic aerosol formation: Explicit modeling of SOA formation from alkane and alkene oxidation. *Atmos. Chem. Phys.* **16,** 1417–1431 (2016).

44. Krechmer, J. E., Pagonis, D., Ziemann, P. J. & Jimenez, J.-L. Quantification of Gas-Wall Partitioning in Teflon Environmental Chambers Using Rapid Bursts of Low-Volatility Oxidized Species Generated in Situ. *Environ. Sci. Technol.* **50,** 5757–5765 (2016).

45. Kulmala, M. *et al.* On the formation, growth and composition of nucleation mode particles. *Tellus, Ser. B Chem. Phys. Meteorol.* **53,** 479–490 (2001).

46. Pagonis, D., Krechmer, J. E., Gouw, J. De, Jimenez, J. L. & Ziemann, P. J. Effects of gas – wall partitioning in Teflon tubing and instrumentation on time-resolved measurements of gas-phase organic compounds. *Atmos. Meas. Tech.* 4687–4696 (2017).

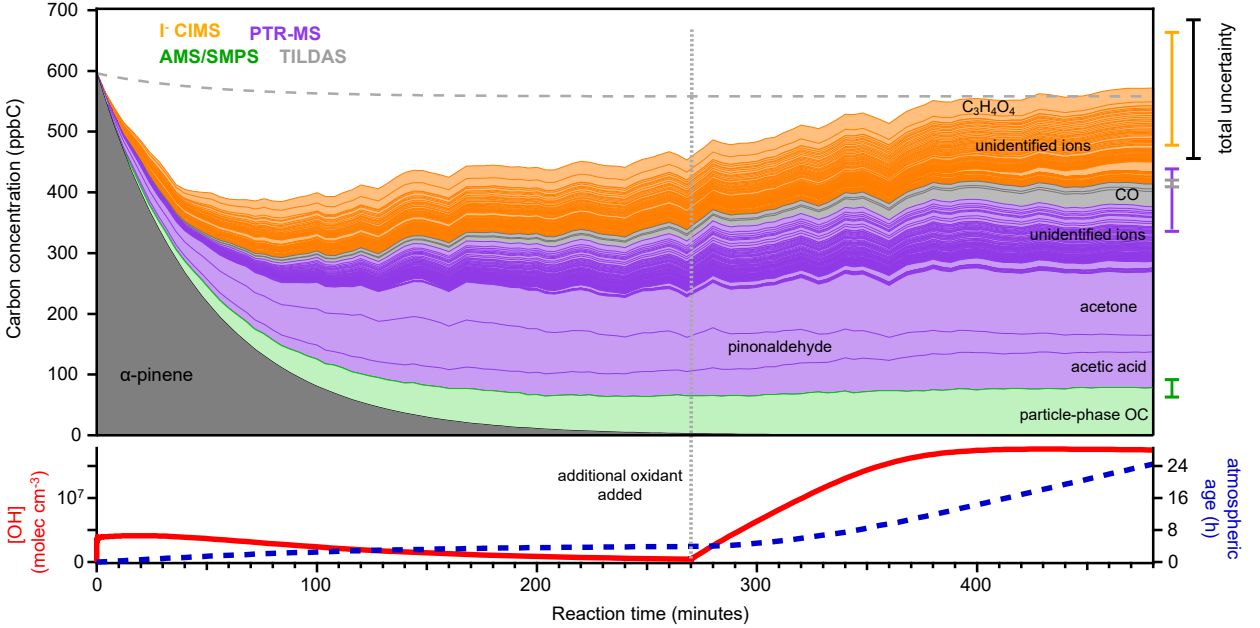
I⁻ CIMS
PTR-MS
AMS/SMPS
TILDAS
Carbon concentration (ppbC)
700
600
500
400
300
200
100
0
α-pinene
$C_3H_4O_4$
unidentified ions
CO
unidentified ions
acetone
pinonaldehyde
acetic acid
particle-phase OC
total uncertainty
additional oxidant added
[OH] (molec cm⁻³)
10^7
0
atmospheric age (h)
24
16
8
0
0
100
200
300
400
Reaction time (minutes)

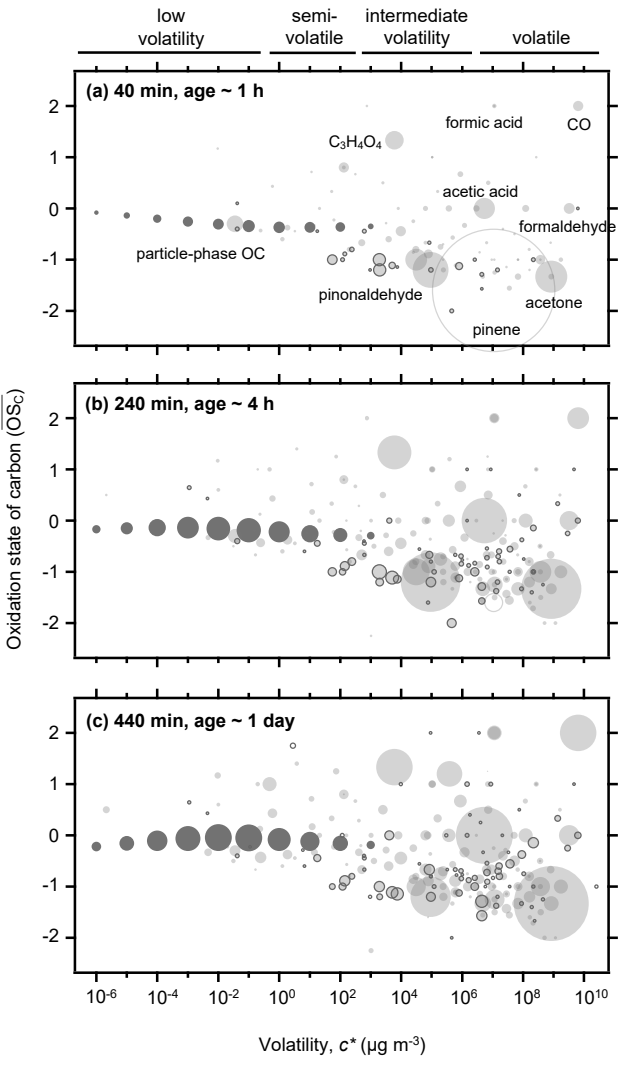
low volatility
semi-volatile
intermediate volatility
volatile
(a) 40 min, age ~ 1 h
(b) 240 min, age ~ 4 h
(c) 440 min, age ~ 1 day
formic acid
CO
$C_3H_4O_4$
acetic acid
formaldehyde
particle-phase OC
pinonaldehyde
acetone
pinene
Oxidation state of carbon ($\overline{OS_C}$)
Volatility, c^* (μg m^{-3})

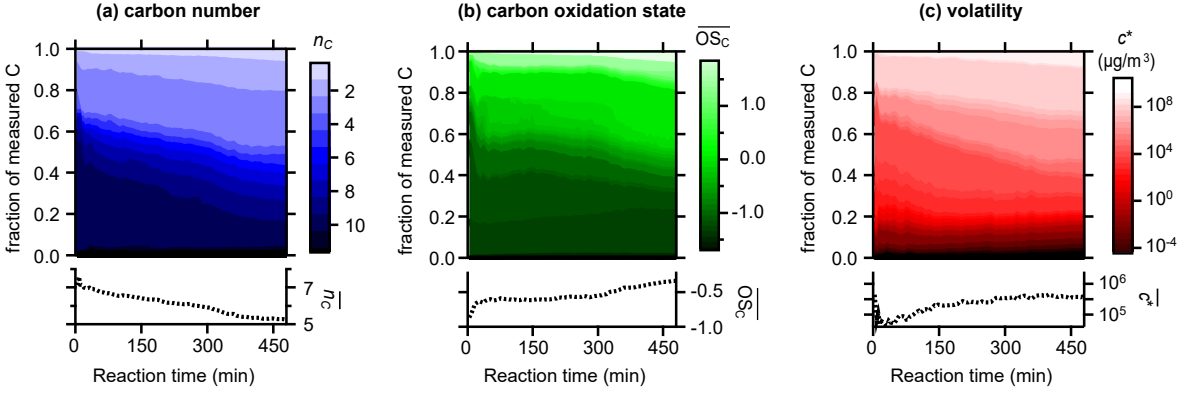
(a) carbon number
n_C
2
4
6
8
10
fraction of measured C
1.0
0.8
0.6
0.4
0.2
0.0
$\overline{n_C}$
7
5
0
150
300
450
Reaction time (min)
(b) carbon oxidation state
$\overline{OS_C}$
1.0
0.0
-1.0
fraction of measured C
$\overline{OS_C}$
-0.5
-1.0
0
150
300
450
Reaction time (min)
(c) volatility
c^*
(μg/m^3)
10^8
10^4
10^0
10^{-4}
fraction of measured C
$\overline{c^*}$
10^6
10^5
0
150
300
450
Reaction time (min)

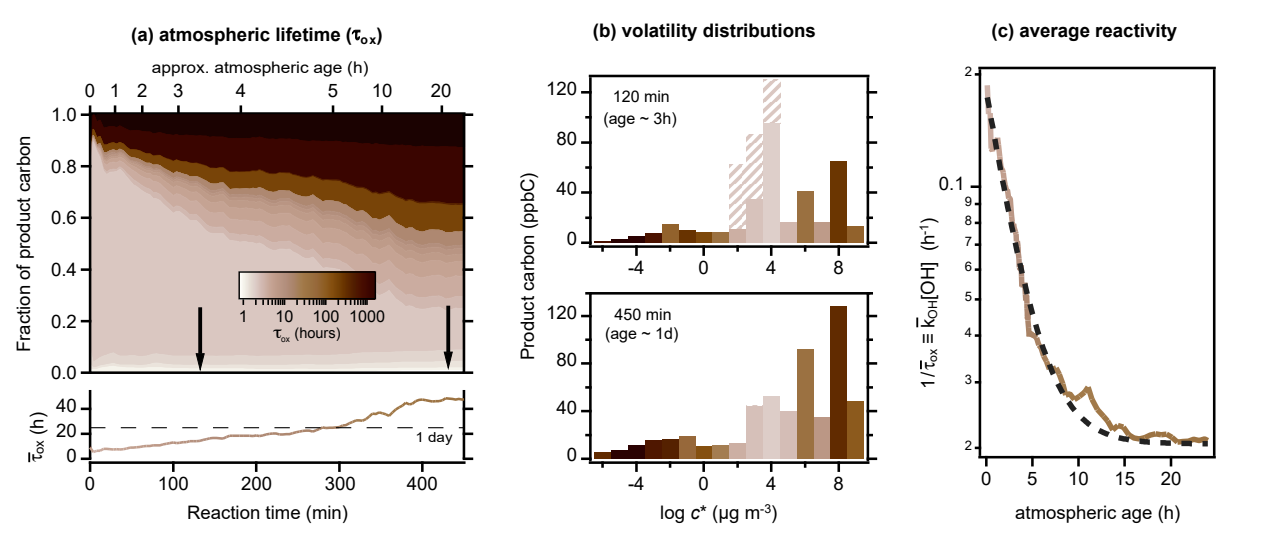
(a) atmospheric lifetime (τ_{ox})
approx. atmospheric age (h)
0 1 2 3 4 5 10 20
Fraction of product carbon
1.0
0.8
0.6
0.4
0.2
0.0
1 10 100 1000
τ_{ox} (hours)
$\bar{\tau}_{ox}$ (h)
40
20
0
1 day
0 100 200 300 400
Reaction time (min)
(b) volatility distributions
120 min
(age ~ 3h)
120
80
40
0
-4 0 4 8
450 min
(age ~ 1d)
Product carbon (ppbC)
log c^* (μg m^{-3})
(c) average reactivity
2
0.1
9
8
7
6
5
4
3
2
$1/\bar{\tau}_{ox} \equiv \bar{k}_{OH}[OH]$ (h^{-1})
0 5 10 15 20
atmospheric age (h)

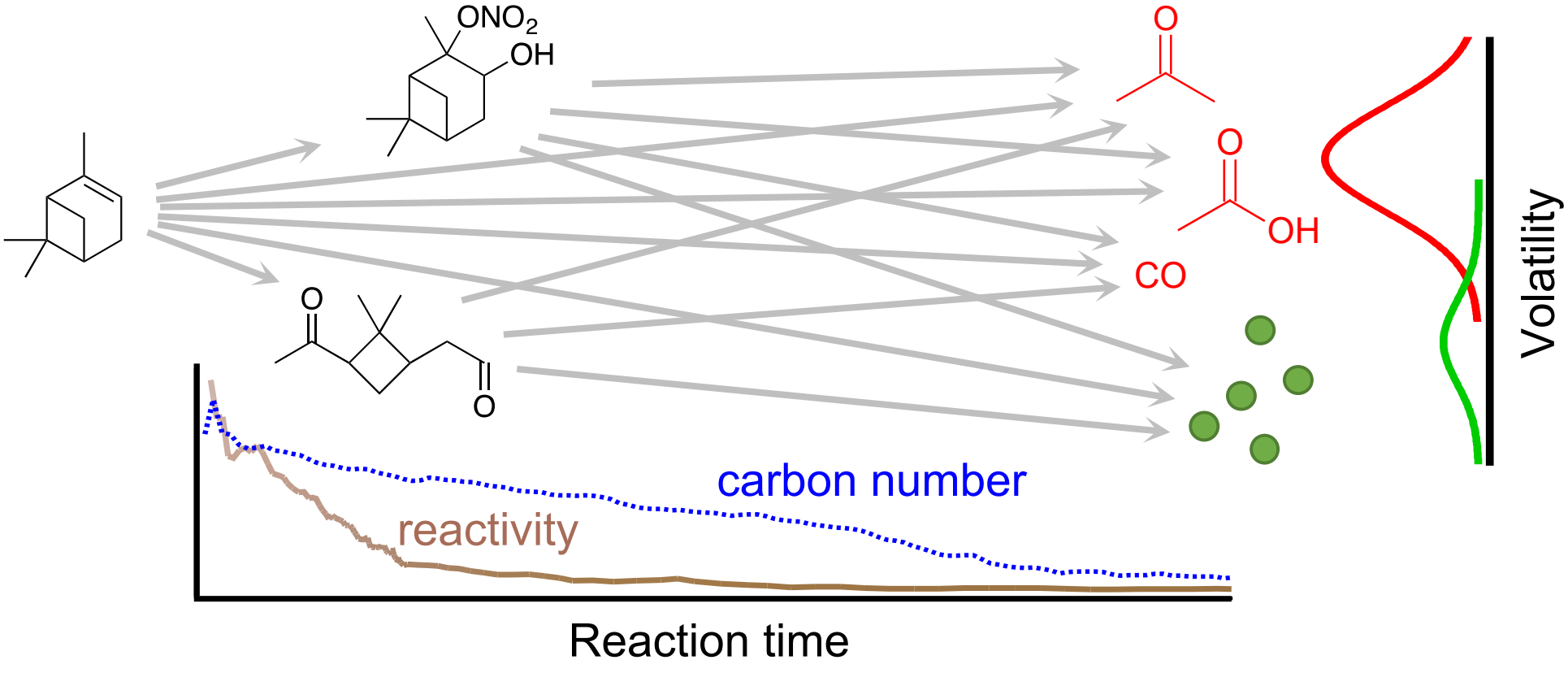
ONO2
OH
O
O
O
OH
CO
O
O
carbon number
reactivity
Reaction time
Volatility